DOE/JPL-956786-86/1
9950-1218

IN-CAT.44
72105-CR
69 P.

Development of High-Efficiency Solar Cells on Silicon Web

D. L. Meier, J. Greggi, and P. Rai-Choudhury

Seventh Quarterly Progress Report
October 1 to December 31, 1985
Contact No. 956786

This work was performed for the
Jet Propulsion Laboratory

March 6, 1986

(NASA-CR-180222) DEVELOPMENT OF HIGH-EFFICIENCY SOLAR CELLS ON SILICON WEB Quarterly Progress Report, 1 Oct. - 31 Dec. 1985 (Westinghouse Research and Development Center) 69 p Avail: NTIS HC A04/MF A01 G3/44
N87-22304
Unclas
0072105

Westinghouse R&D Center
1310 Beulah Road
Pittsburgh, Pennsylvania 15235

This report was prepared for the Jet Propulsion Laboratory, California Institute of Technology, sponsored by the National Aeronautics and Space Administration.

Development of High-Efficiency Solar Cells on Silicon Web

D. L. Meier, J. Greggi, and P. Rai-Choudhury

Seventh Quarterly Progress Report
October 1 to December 31, 1985
Contact No. 956786

This work was performed for the
Jet Propulsion Laboratory

March 6, 1986

Westinghouse R&D Center
1310 Beulah Road
Pittsburgh, Pennsylvania 15235

Table of Contents

List of Figures.. iii

List of Tables... vii

Abstract ix

1. Summary... 1

2. Introduction 5

3. Technical Progress 7

  3.1 Cross-Sectional TEM Analysis Of Completed Web Cells 7

    3.1.1 Twin Lamellae Terminating Within the Bulk of Cell 30A (14.4%) 7

    3.1.2 Asymmetric Distribution of Dislocations in Cell 41A (12.0%) 14

    3.1.3 Additional TEM Images for Cells 40C (10.0%) and 69A (14.3%) 18

    3.1.4 Evidence of Dislocation Climb in Cell 17C (9.5%) 18

  3.2 Modelling The Heavily Twinned Region.................... 23

    3.2.1 Hydrogen Ion Implantation Into Web Cells Using the Westinghouse System 28

  3.3 Cell Fabrication 38

    3.3.1 Web and Float-Zone Cells Without Oxide Passivation 39

    3.3.2 Web and Float-Zone Cells With Oxide Passivation .. 45

  3.4 Design Of a Grid System With Reduced Metal/ Silicon Contact Area.................................... 51

  3.5 Verification of DLTS Measurement Technique For Beveled Samples 53

4. Program Status 55

  4.1 Present Status 55

  4.2 Future Activity 57

5. References 59

6. Acknowledgments 60

List of Figures

Figure	Title	Page
1.	Cross-sectional TEM micrographs of Section 1 of cell 30A with the twin planes vertical showing the presence of three twin boundaries: (a) bright-field, (b) dark-field, and (c) dark-field with higher magnification...	9
2.	Cross-sectional TEM micrographs of Section 1 on cell 30A with the twin planes tilted. No dislocations are observed..	11
3.	Cross-sectional TEM micrographs of Section 2 of cell 30A showing the presence of two additional twinned regions..	12
4.	Cross-sectional TEM micrographs of Section 2 of cell 30A with the twin planes tilted. A high density of dislocations is associated with the formation of the additional twinned regions and with the distortion of the original twin boundary.........................	13
5.	Cross-sectional TEM micrographs of Section 3 of cell 30A showing seven twin boundaries and the distribution of dislocations, many of which are decorated with impurity precipitates..............................	15
6.	Cross-sectional TEM micrographs of cell 41A showing a large number of twin boundaries and very thin twin lamellae..	16
7.	Cross-sectional TEM micrographs of cell 41A showing an asymmetric distribution of dislocations within the heavily twinned region............................	17
8.	Cross-sectional TEM micrographs of cell 40C showing the formation of dislocation networks....................	19
9.	Cross-sectional TEM micrographs of cell 69A with the twin planes vertical..............................	20
10.	Cross-sectional TEM micrographs of cell 69A with the twin planes tilted................................	21

List of Figures (Cont.)

Figure	Title	Page
11.	Cross-sectional TEM micrographs of cell 17C showing dislocation climb and the trail of precipitates left behind..	22
12.	Modeling the effect of the heavily twinned region on cell efficiency................................	25
13.	Quantum efficiency curves calculated including a heavily twinned region located midway through the cell thickness having a width of 6 μm and a diffusion length of 1 μm. Cell thickness is 150 μm and the base diffusion length is a parameter..................................	26
14.	Quantum efficiency curves calculated ignoring heavily twinned region. Cell thickness is 150 μm and the base diffusion length is a parameter.....................	27
15.	Schematic diagram of Veeco Microetch system adapted for low-energy, high-dose hydrogen ion implantation...	31
16.	Photograph of the Veeco Microetch system which has been made available for hydrogen ion implantation at the Westinghouse R&D Center.........................	32
17.	Photograph of a web cell being mounted for hydrogen ion implantation..	34
18.	Photograph of web cell during hydrogen ion implantation (the light for exposing the photographic film came from a violet glow associated with the hydrogen ion beam)..	35
19.	Measured reflectivity for web cell 61B-3 after the deposition of the antireflection coating (600 Å ZnS and 1000 Å MgF_2) on bare (unpassivated) silicon. The cell has a 1000 Å evaporated aluminum back-surface reflector. (Run Cell-1)............................	43
20.	Measured quantum efficiency for web cell 61B-3 after the deposition of the antireflection coating (600 Å ZnS and 1000 Å MgF_2) on bare (unpassivated) silicon. The cell has a 1000 Å evaporated aluminum back-surface reflector. (Run Cell-1)............................	44

List of Figures (Cont.)

Figure | Title | Page

21. Diffusion length plot constructed from quantum efficiency data for web cell 61B-3 showing the effective increase in minority carrier diffusion length with wavelength. (Run Cell-1) 46

22. Dopant profile for the front (n^+p) junction of partial web cell 61B-4 by spreading resistance. (Run Cell-1) 47

23. Dopant profile for the back (p^+p) region of partial web cell 61B-4 by spreading resistance. (Run Cell-1) 48

24. Process sequence for metal contact to silicon along grid line openings in oxide 49

25. Process sequence for metal contact to silicon at dot openings in oxide only 52

26. DLTS scan (C_{56}) for a Schottky diode (stripe) on the beveled surface of a sample prepared from an unprocessed Ti-doped CZ wafer (ingot 210-Ti, boron-doped to 4 ohm-cm). (Run TP-12, Sample #11, Stripe #2) 54

List of Tables

Table Title Page

1. Electrical Parameters of Cells Examined by Cross-Sectional TEM.......... 8

2. Effect of Heavily Twinned Region on Cell Parameters... 29

3. Implantation Parameters for the Hydrogen Ion Implanter at the Westinghouse R&D Center.......... 30

4. Conditions for H^+ Implantation into Web Cells......... 36

5. Effect of H^+ Implantation on Web Cell Parameters...... 37

6. Lighted I-V and Diffusion Length Data for Web and Float-Zone Silicon Cells Before and After Double-Layer Antireflection Coating. (Run Cell-1).......... 40

7. Ratio of Cell Parameters After AR Coating to Cell Parameters Before AR Coating (Run Cell-1).......... 42

8. Dark I-V Parameters for High-Efficiency Web Cells (Run Cell-1).......... 42

9. Lighted I-V Data for Oxide-Passivated Web and Float-Zone Silicon Cells Before and After Double-Layer Antireflection Coating. (Run Cell-1).......... 50

10. Milestone Chart.......... 56

Abstract

This seventh quarterly report describes the results of work aimed at identifying and reducing sources of carrier recombination both in the starting web silicon material and in the processed cells. Cross-sectional TEM measurements of several web cells have been made and analyzed. The effect of the heavily twinned region on cell efficiency has been modeled, and the modeling results compared to measured values for processed cells. The effects of low-energy, high-dose hydrogen ion implantation on cell efficiency and diffusion length have been examined. Cells have been fabricated from web silicon known to have a high diffusion length, with a new double-layer antireflection coating being applied to these cells. A new contact system, to be used with oxide-passivated cells and which greatly reduces the area of contact between metal and silicon, has been designed. Finally, the application of DLTS measurements to beveled samples has been further investigated.

1. Summary

The major objective of this contract is to improve web base material with a goal of obtaining solar cell efficiencies in excess of 18% (AM1). Efforts in this program are directed toward identifying carrier loss mechanisms in web silicon, eliminating or reducing these mechanisms, designing a high-efficiency cell structure with the aid of numerical models, and fabricating high-efficiency web solar cells. Fabrication techniques must preserve or enhance carrier lifetime in the bulk of the cell and minimize recombination of carriers at the external surfaces.

In the previous quarterly progress report for this program, factors limiting the diffusion length in dendritic web silicon solar cells were discussed. TEM, SPV, LBIC, and DLTS measurements have provided convincing evidence that dislocations which are decorated with impurity precipitates, or perhaps the dislocations themselves, are acting to limit the diffusion length. Since processing temperatures are not sufficiently high to create dislocations in silicon, it is thought that the dislocations, and probably also the impurity precipitates, are introduced into the web material during its growth from the melt. The concentration of these dislocations and precipitates is significantly higher in the heavily twinned region than it is in the remainder of the bulk silicon. During this reporting period, cross-sectional TEM analysis has been completed for two web cells (30A and 41A) that were fabricated with the baseline processing sequence at AESD. Improved TEM images have also been obtained for cells which had been examined previously (40C, 69A, and 17C).

The TEM images from Cell 30A, which had an efficiency of 14.4%, showed for the first time that twin planes can terminate within the bulk crystal rather that at the dendrites. The number of twin planes changed from three to seven in one of the cross-sectional TEM samples that was examined from this cell. This change was accompanied by a high local density of dislocations as the crystal accommodated the additional lamellae. Furthermore, the original twin boundary nearest the additional twins deformed somewhat in the vicinity of these additional twins. The region of the crystal which had only three twin boundaries showed no dislocations, thereby placing the dislocation density below the TEM detection limit of 10^4 to 10^5 cm^{-2}. However, the region of the crystal with seven twin boundaries had a dislocation density of 2.9×10^7 cm^{-2} within the heavily twinned region. This suggests that the electrical quality (minority carrier diffusion length) may not be uniform in cell 30A. Growth conditions which give rise to twin boundaries terminating within the bulk crystal may be associated with a degradation of electrical quality.

Web cell 41A, which had an efficiency of 12.0%, had a large number of twin boundaries (perhaps 37) grouped into two bands. Some of the crystal lamellae were extremely thin (<500 Å). The dislocations in the heavily twinned region were distributed very asymmetrically, with most present within one of the two bands. This suggests a nonsymmetric stress distribution in the growing web.

Dislocation networks, rather than individual dislocations, have been observed in a thick portion of a TEM sample for web cell 40C, which had an efficiency of 10.0%. Evidence of the climb of a dislocation in the bulk of web cell 17C, which had an efficiency of 9.5%, is also presented. A TEM analysis of this cell has already been described in previous reports. However, the TEM image of a trail of impurity precipitates, indicating the movement of the dislocation, is new.

The effect of the heavily twinned region on cell parameters and on the spectral response of the cells has been modeled. The heavily twinned region was represented as a slab of material 6 μm thick located midway through the thickness of the web cell, and having a diffusion length of 1 μm. The diffusion length of the remainder of the base was varied from 10 μm to 300 μm. It was found that the presence of the heavily twinned region is not important when the base diffusion length is considerably less than the depth of that region. However, when the diffusion length exceeds that depth, then the presence of the heavily twinned region is strongly felt. The measured efficiency of web cells that have been examined by TEM and LBIC measurements agrees well with the values calculated from the model.

A system for implanting a low-energy, high-dose of hydrogen ions into dendritic web cells has been made available at the Westinghouse R&D Center. With this system a significant improvement in the efficiency and diffusion length of some web cells has been obtained. Implantation at an energy of 1500 eV, a beam current density of 2 mA/cm^2, and a time of 2 minutes has resulted in the largest improvement thus far. The best result was for a web cell in which the efficiency was increased from 8.0% (no AR coating) to 9.8%. The diffusion length for this cell also increased from 23 μm to 58 μm as a result of the implantation.

During this reporting period emphasis has also been placed on fabricating cells from web material which has been selected to be of superior electrical quality, with measured diffusion lengths approaching the web thickness. Web cells having an area of 4 cm^2, as required by the program, have been fabricated in some cases. Superior quality web material was assured by starting with a cell which was fabricated by the baseline processing sequence at AESD with an efficiency of 15.5% and then stripping the metal and single-layer AR coating from it. With the application of an aluminum back-surface reflector and a double-layer AR coating, three web cells, each with an area of 1 cm^2, were obtained with efficiencies exceeding 17%, as measured at the Westinghouse R&D Center. The areas were defined by a mesa etch. The highest efficiency was 17.3%. This represents an advance over the previous highest efficiency of 16.9% for a web cell which also had a mesa-defined area of 1 cm^2 and was measured in the same way. The high efficiency is attributed to a significant increase in current because of a very effective double-layer AR coating and an aluminum back-surface reflector. ZnS and MgF_2 comprise the two layers of the AR coating. ZnS replaced the ZnSe which was used in an earlier coating because ZnSe was found to absorb light with a wavelength below 500 nm. ZnS is transparent to all wavelengths of light in the usable solar spectrum. Enhancements of short-circuit current of

51% and efficiency of 55%, compared to a bare silicon surface, are attributed to this coating. Oxide passivation of both the front and back surfaces was also included in the processing of some web and float-zone cells. The open-circuit voltage of these cells without the AR coating was usually somewhat greater than for the comparable nonpassivated cells. However, after the double-layer AR coating, the efficiency was not as high as for the nonpassivated cells. This is primarily a result of the nonoptimum thicknesses of ZnS and MgF_2 deposited on the thin passivating SiO_2 layer.

A mask was designed in which the metal/silicon contact area is reduced by a factor of 40 compared to the present design. This is expected to reduce the recombination in the vicinity of the metal/silicon interface, and therefore to increase the short-circuit current and open-circuit voltage, especially for cells with a low-resistivity (0.2 ohm-cm) base. Calculations of the contribution of the contact resistance to the total series resistance indicate that this reduction will not degrade the series resistance, provided the doping concentration of the n-type emitter at the silicon surface exceeds 10^{19} cm^{-3}.

Finally, a beveled sample, prepared from an unprocessed CZ wafer which had titanium grown-in from the melt, was examined using DLTS. This sample served as a calibration standard, and the DLTS measurements verified that Sirtl etching is effective in removing the surface damage caused by the beveling. The DLTS scan was free from artifacts, and the energy level and concentration of titanium obtained from Schottky diodes in the shape of stripes agreed with previous values obtained by conventional DLTS dots.

2. Introduction

The idealized efficiency of a silicon solar cell is about 25%, although present day cells fall considerably short of this limiting value. This is largely a consequence of heavy doping effects, nonideal bulk parameters (particularly minority carrier diffusion length), and high recombination at the cell surfaces. The major problems of efficiency improvements fall in the above categories. In addition, efficient contacts and antireflection coatings are essential and must be optimized consistent with device structure.

Starting material is vitally important for high-efficiency cells, since high efficiency (>17%) cannot be realized if the starting material is poor or if it degrades with processing. The objective of this program is to understand and improve web silicon so that high-efficiency web cells can be fabricated using advanced cell design and processing. This includes the understanding of mechanisms which limit the diffusion length in web silicon, the development of means for eliminating or ameliorating these mechanisms, the recognition of excessive recombination activity in all regions of an operating cell, and the reduction of this recombination.

This seventh quarterly report describes the results of work aimed at identifying and reducing sources of carrier recombination both in the starting web silicon material and in the processed cells. Toward that end, cross-sectional TEM measurements of several web cells have been made and analyzed. The effect of the heavily twinned region on cell efficiency has been modeled, and the modeling results compared to measured values for processed cells. The effects of low-energy, high-dose hydrogen ion implantation on cell efficiency and diffusion length has been examined. Cells have been fabricated from web silicon, known to have a high diffusion length, with a new double-layer antireflection coating being applied to these cells. A new contact system, to be used with oxide-passivated cells, which greatly reduces the area of contact between metal and silicon has been designed. Finally, the application of DLTS measurements to beveled samples has been further investigated.

3. Technical Progress

3.1 CROSS-SECTIONAL TEM ANALYSIS OF COMPLETED WEB CELLS

In previous progress reports, the results of cross-sectional TEM analysis of four web cells (40C, 69A, 17C, and 38A) were presented, along with the data from relevant electrical measurements. In this report, results for two additional cells (41A and 30A) are given, as well as some improved TEM images of the original four cells. The electrical parameters for the six cells under consideraton are summarized in Table 1.

3.1.1 Twin Lamellae Terminating Within the Bulk of Cell 30A (14.4%)

From Table 1 it can be seen that Cell 30A has an efficiency of 14.4%, which is higher than the average of 14.0% for cells produced using the baseline processing sequence at AESD. Three adjacent pieces, each 2.4 mm square, were cut along the length of the cell and examined by TEM. Each of the three sections exhibits different structural features. The three images, taken as a whole, provide a record of a structural configuration in web which was previously not known.

Figures 1a and 1b show a bright-field (BF) and a dark-field (DF) cross-sectional view of Section 1 of Cell 30A, with the twin planes vertical. Figure 1c is a dark-field image at higher magnification, as indicated by the scale marker in the micrograph. A dark-field image clearly distinguishes between that part of the crystal which has the orientation of the matrix (light bands) and that part in which the orientation is twin-related to the matrix (dark bands). As can be seen from Figures 1b and 1c, there are only three twin boundaries in this section of the web crystal, with the extreme boundaries separated by 3.6 μm. A bright-field image is useful for examining the twin boundaries for evidence of additional defects which might be lying in

Table 1. Electrical Parameters of Cells Examined by Cross-Sectional TEM

Cell	Crystal	Processing Run	L_n(SPV) (μm)	J_{sc} (mA/cm^2)	V_{oc} (V)	FF	η (%)
40C	2-287-4.2	5204-25W	19	24.3	0.525	0.78	10.0
69A	5-232-12.4	0623-49W	135	31.2	0.580	0.78	14.3
17C	J-546-2.2	5110-1W	12	23.4	0.514	0.79	9.5
38A	2-292-4.3	T5312-25E	156	31.0	0.584	0.79	14.9
41A	6-302-5	T5312-25E	16	27.7	0.548	0.78	12.0
30A	R-474-7.4	4N01-25E	70	30.2	0.585	0.78	14.4

Notes:

1. Cells have p-base (boron-doped) of nominal 4 ohm-cm resistivity.
2. Cell size is (2.0 x 9.8) cm or (2.5 x 9.8) cm.
3. Cells tested at 100 mW/cm^2, AM1 spectrum at room temperature.

CELL 30A HIGH EFFICIENCY (14.4%)

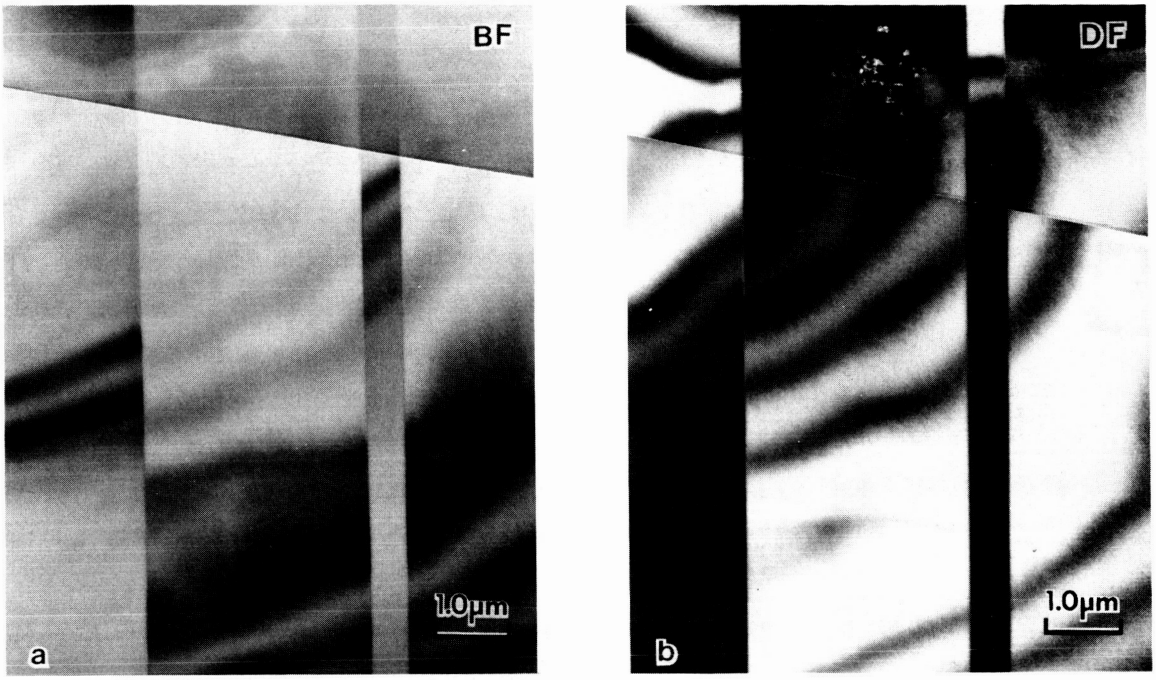

Twin Plane Vertical

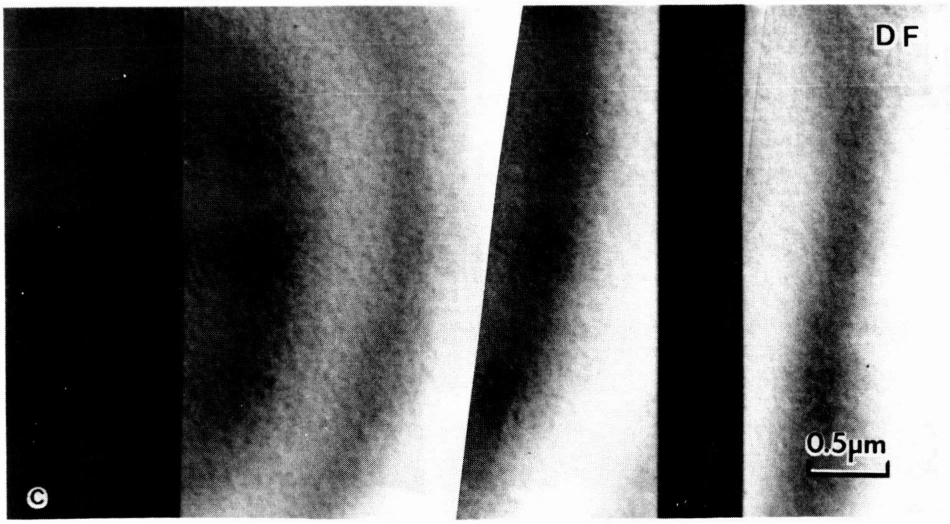

Figure 1. Cross-sectional TEM micrographs of Section 1 of cell 30A with the twin planes vertical showing the presence of three twin boundaries: (a) bright-field, (b) dark-field, and (c) dark-field with higher magnification.

the plane of the twin boundary. Figure 1a gives no indication of the presence of such additional defects.

In order to examine the twin boundaries more carefully for defects, the sample is tilted and imaged in the bright-field mode. Such imaging, done with magnifications of 10,000X and 20,000X, are given in Figure 2. There the twin boundaries in Section 1 are shown to be free from defects, particularly dislocations. The parallel lines that appear near a twin boundary in the tilted view are fringes associated with the interference of the electron beam reflected from the surface of the sample with the electron beam reflected from the twin plane. These can be seen most easily in Figure 2c. Thus, Section 1 of Cell 30A is characterized by three twin boundaries which are free from dislocations.

A cross-sectional view of Section 2 (adjacent to Section 1) of Cell 30A with the twin planes vertical is given in Figure 3. Figure 3a (10,000X) shows three twin boundaries to the left, as were found for Section 1. However, near the right side of Figure 3a, two additional twinned sections (four additional twin boundaries) have formed. This formation is accompanied by a high density of dislocations, as shown in Figures 3b (20,000X) and 3c (60,000X). It can also be seen that the original twin boundary near the additional twinned regions is affected by their presence, since this original boundary moves somewhat closer to the new twins.

When Section 2 of cell 30A is tilted in order to bring the dislocations into contrast, the images given in Figure 4 are obtained. Figures 4a, 4b, and 4c correspond to Figures 3a, 3b, and 3c, respectively. It is apparent that a very high density of dislocations are created both at the ends of the additional twinned regions and at the location where the original twin boundary becomes distorted. This is the first observation of the termination of twinned regions in the bulk of silicon web. This shows that the multiple twin boundaries that have been seen recently in web cells need not originate in the seed used

ORIGINAL PAGE IS
OF POOR QUALITY

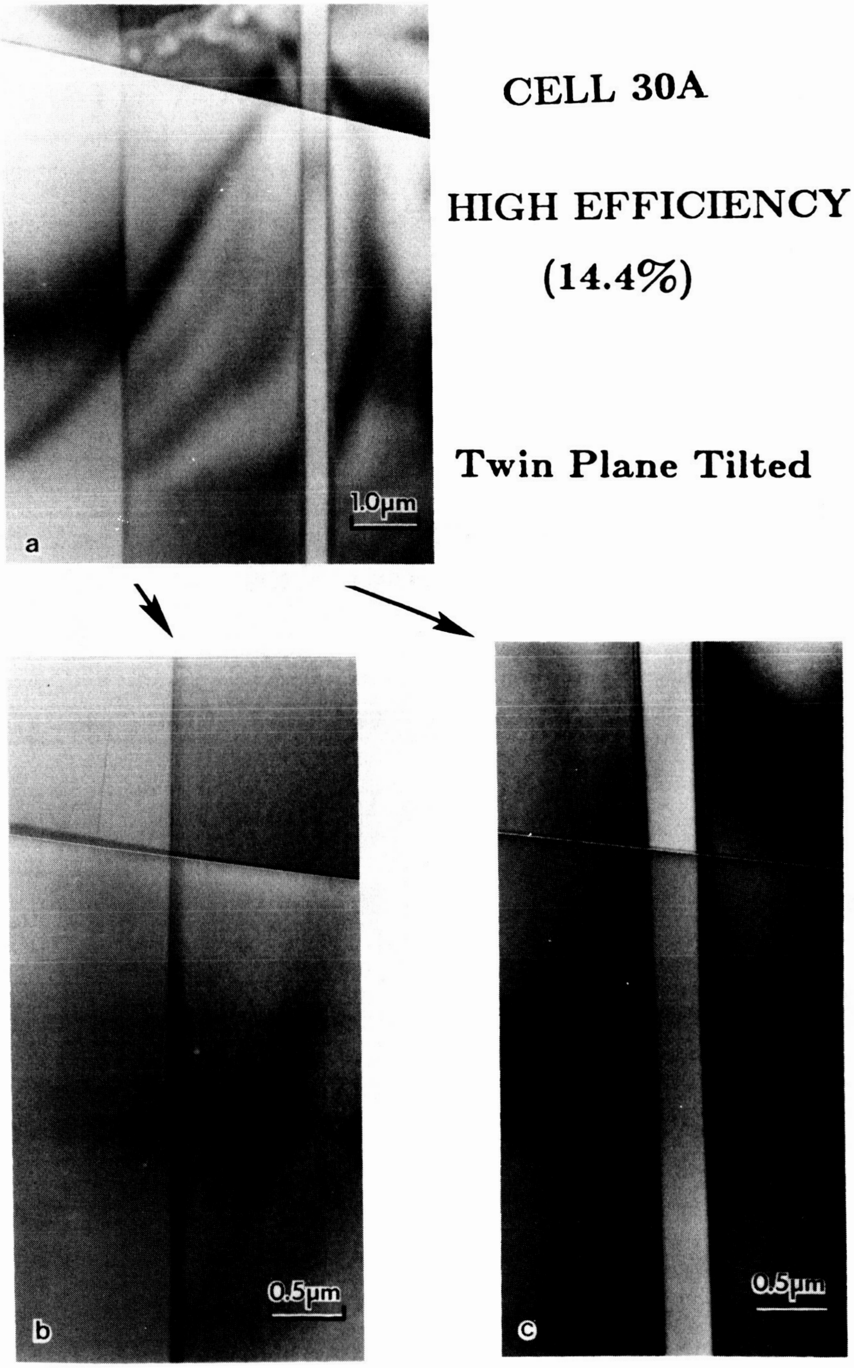

CELL 30A

HIGH EFFICIENCY
(14.4%)

Twin Plane Tilted

Figure 2. Cross-sectional TEM micrographs of Section 1 on cell 30A with the twin planes tilted. No dislocations are observed.

CELL 30A HIGH EFFICIENCY (14.4%)

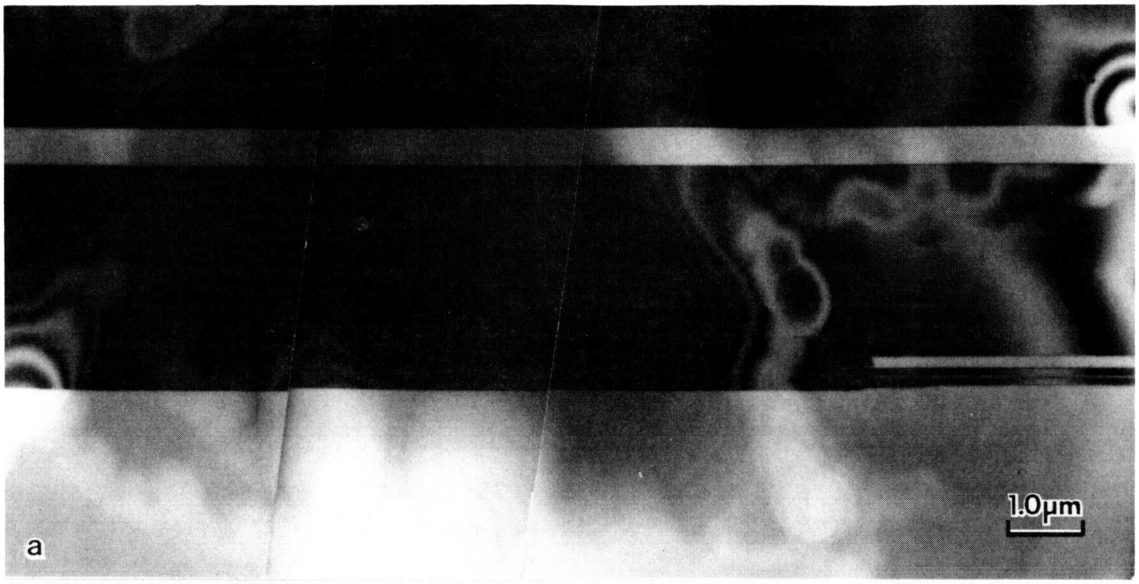

Twin Plane Vertical

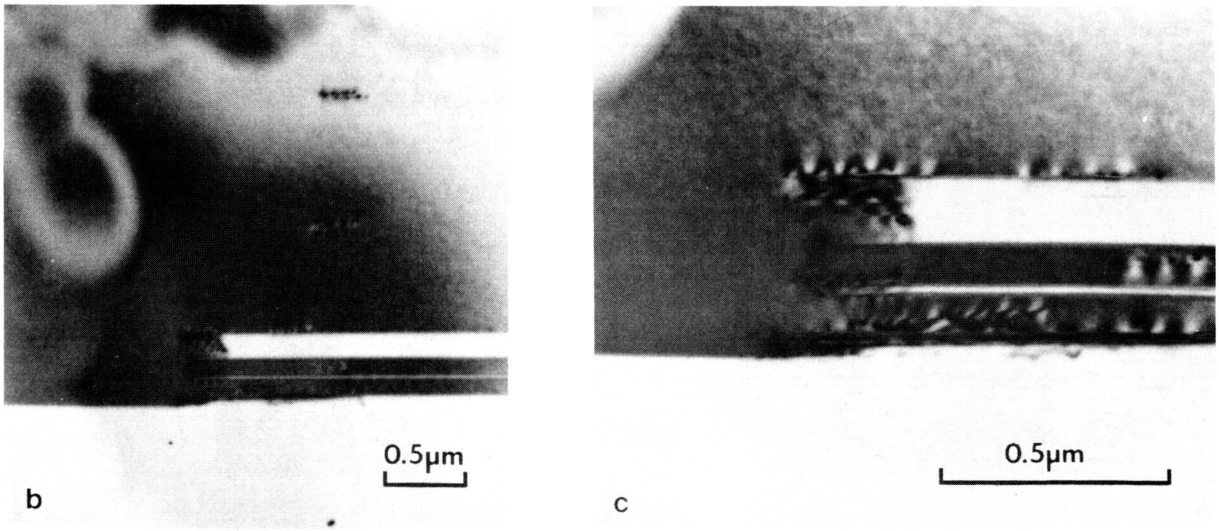

Figure 3. Cross-sectional TEM micrographs of Section 2 of cell 30A showing the presence of two additional twinned regions.

CELL 30A HIGH EFFICIENCY (14.4%)

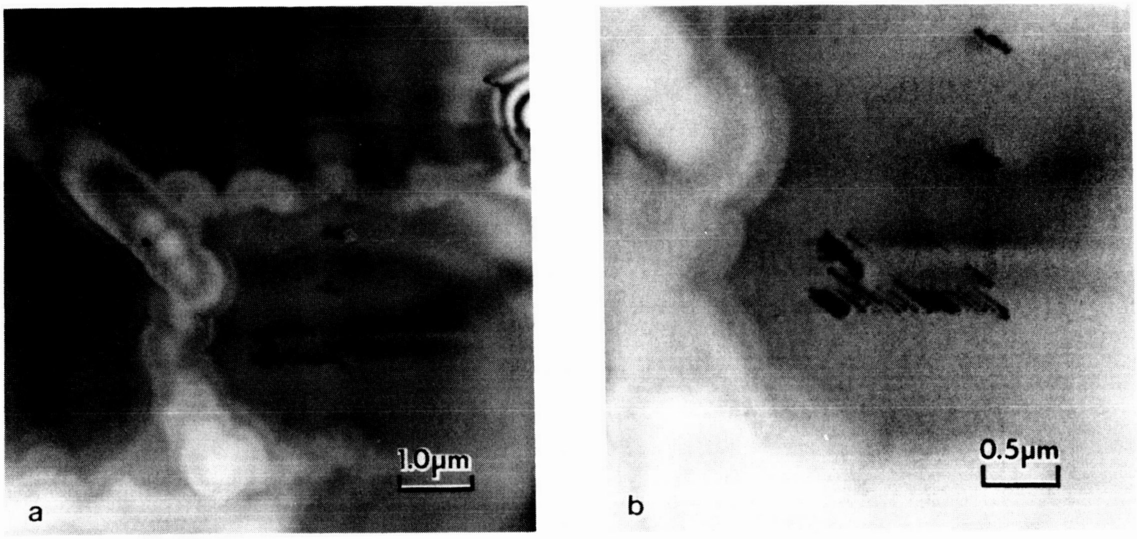

Twin Plane Tilted

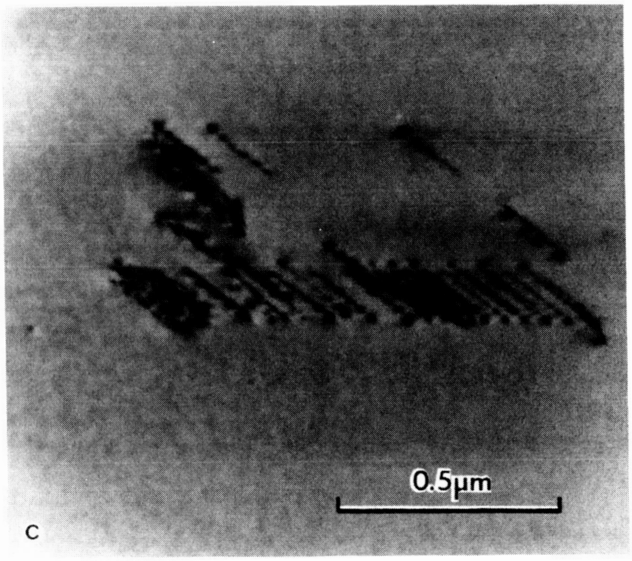

Figure 4. Cross-sectional TEM micrographs of Section 2 of cell 30A with the twin planes tilted. A high density of dislocations is associated with the formation of the additional twinned regions and with the distortion of the original twin boundary.

to initiate web growth. It is perhaps fortuitous that the particular section of the web crystal in which the twin boundaries terminated was part of the TEM specimen. However, it suggests that such an event may not be exceedingly rare in the web growth.

Finally, cross-sectional TEM views of Section 3 (adjacent to Section 2) of Cell 30A are given in Figure 5. Figure 5a shows the additional two twinned regions near the bottom of the micrograph and along the entire length. The tilted view, given in Figure 5b, shows a fairly high concentration of dislocations along the outer twin boundary closest to the side where the new twinned regions are located. The other outer twin boundary, marked by an arrow in Figure 5b, has a considerably lower dislocation density. The dislocation density averaged over the entire heavily twinned region is 2.9×10^7 cm^{-2}. A large fraction of the dislocations is decorated with impurity precipitates. Decorated dislocations can also be seen in the bulk, away from the twin boundaries, in Figure 5b.

3.1.2 Asymmetric Distribution of Dislocations in Cell 41A (12.0%)

Cell 41A, which has an intermediate efficiency for the group of cells given in Table 1, was also examined by TEM. Figure 6 shows bright-field and dark-field images with the twin planes vertical. There are a very large number of twin boundaries (perhaps 37), and some of the twin lamellae are extremely thin (< 500 Å). The distance between the extreme twin boundaries is 3.6 µm.

Figure 7a shows the dislocation structure adjacent to the twin boundaries in cell 41A. The dislocations are distributed very asymmetrically, with most occurring within one of the two heavily twinned bands. The other heavily twinned band, marked by an arrow in Figure 7a, has very few dislocations. The average dislocation density within the 3.6 µm wide heavily twinned region of Figure 7a is 9×10^7 cm^{-2}. This is somewhat less than the value found for cells 40C and 17C of Table 1, which was 3×10^8 cm^{-2}, as reported earlier.

ORIGINAL PAGE IS
OF POOR QUALITY

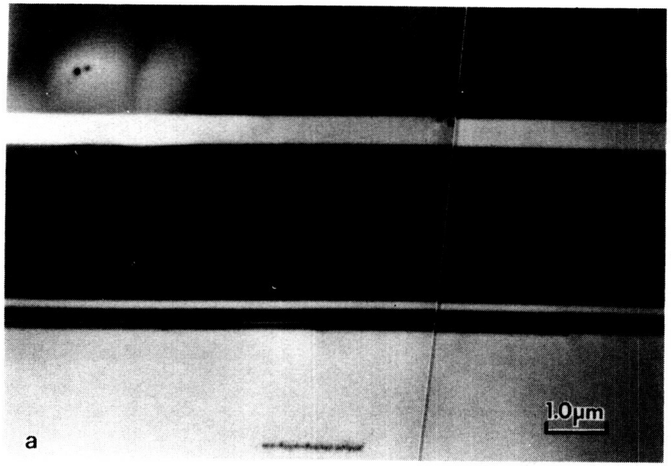

CELL 30A

HIGH EFFICIENCY
(14.4%)

Twin Plane Vertical

Twin Plane Tilted

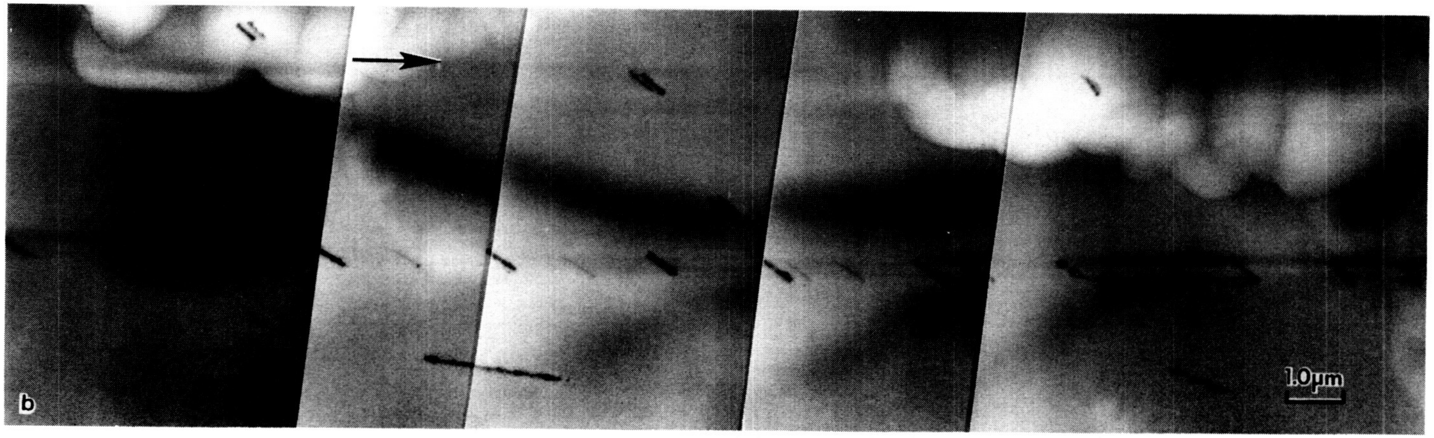

Figure 5. Cross-sectional TEM micrographs of Section 3 of cell 30A showing seven twin boundaries and the distribution of dislocations, many of which are decorated with impurity precipitates.

CELL 41A INTERMEDIATE EFFICIENCY (12.0%)

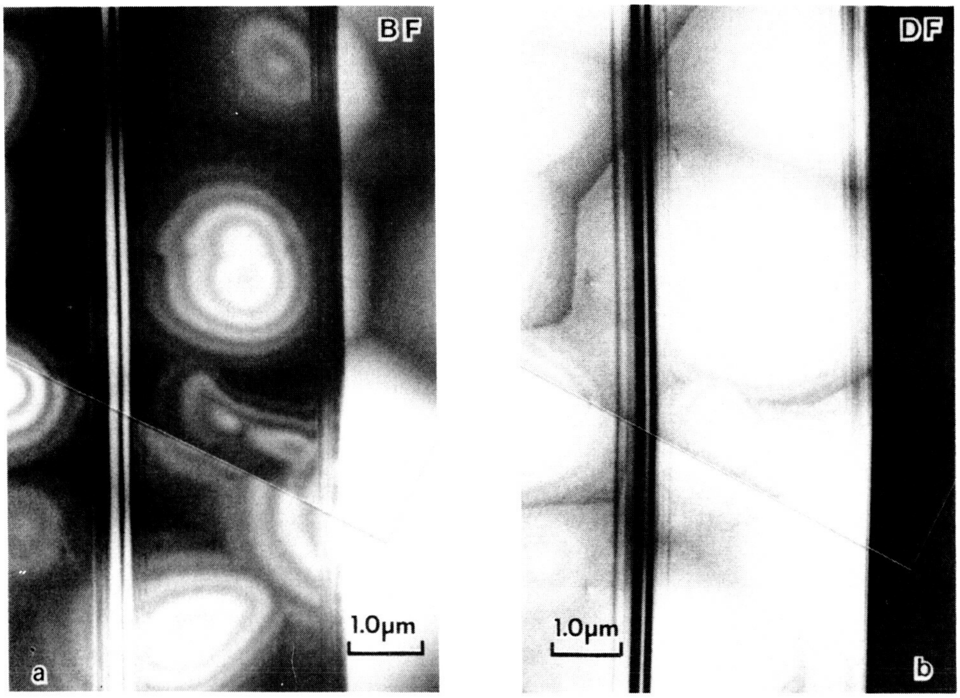

Twin Plane Vertical

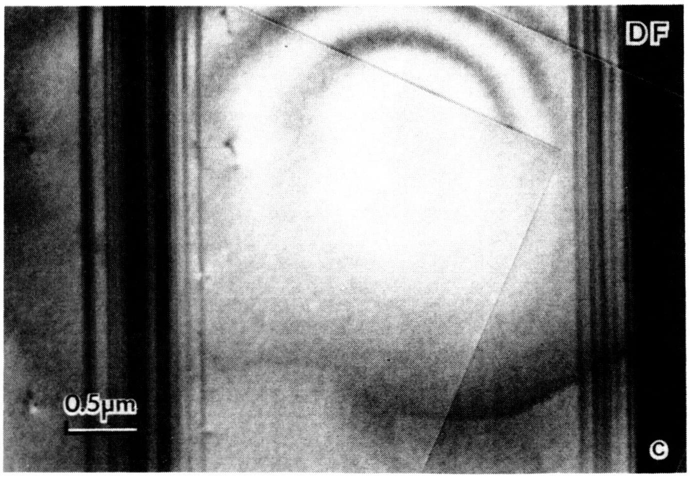

Figure 6. Cross-sectional TEM micrographs of cell 41A showing a large number of twin boundaries and very thin twin lamellae.

CELL 41A INTERMEDIATE EFFICIENCY (12.0%)

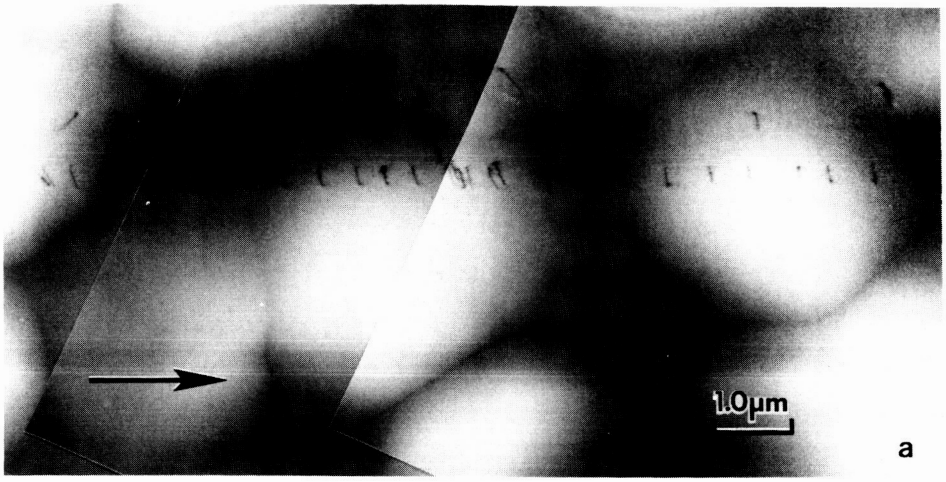

Twin Plane Tilted

Bulk Si-Web Structure

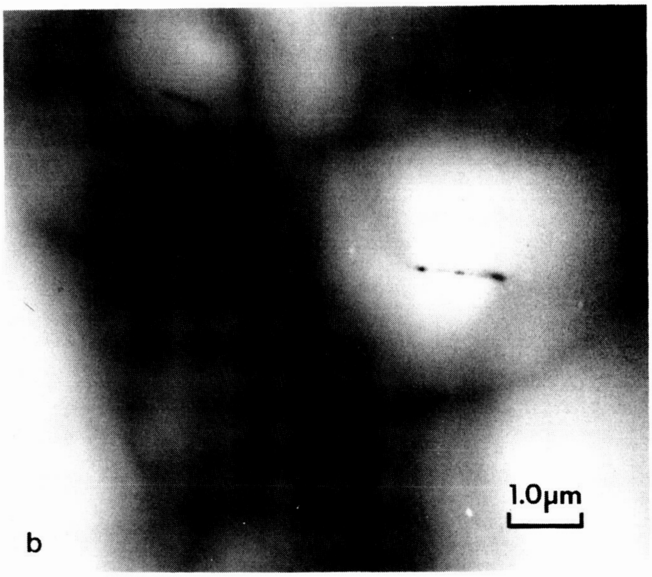

Figure 7. Cross-sectional TEM micrographs of cell 41A showing an asymmetric distribution of dislocations within the heavily twinned region.

Figure 7b shows the bulk structure away from the heavily twinned region, and indicates that dislocations are present at a reasonbly high level in this cell.

3.1.3 Additional TEM Images for Cells 40C (10.0%) and 69A (14.3%)

TEM results for cells 40C and 69A have been presented in the previous quarterly report. However, additional details or higher quality images for these cells have recently been obtained. Figure 8 shows a tilted view of two different sections of Cell 40C. (A section is a square 2.4 mm on a side that was cut from the cell.) The magnification is such that only a portion of the heavily twinned region can be included in each case. The image in Figure 8b is from a thick portion of the TEM specimen and indicates that dislocation networks are being formed. Decorated dislocations are observed frequently.

Figure 9 shows bright-field and dark-field images of cell 69A with the twin planes vertical. Each region with the same crystallographic orientation is marked "T" in the dark-field micrograph. Figure 10 shows the same area as shown in Figure 9, but with the twin planes tilted to illustrate the absence of dislocations in this cell. Figures 10b and 10c are micrographs of the boundary regions at a higher magnification than in Figure 10a.

3.1.4 Evidence of Dislocation Climb in Cell 17C (9.5%)

Figure 11 shows dislocations in two regions of cell 17C. In Figure 11a the heavily twinned region is marked with an arrow, and dislocations in this region are evident. Two dislocations in the bulk are shown in Figure 11b, and one of these dislocations is shown with greater magnification in Figure 11c. The important feature of Figure 11c is that the precipitates and the dislocation do not all coincide. This indicates that the dislocation has climbed, leaving behind a trail of impurity precipitates.

There appear to be three distinct patterns, or tracks, of precipitates, including those precipitates which decorate the

CELL 40C LOW EFFICIENCY (10.0%)

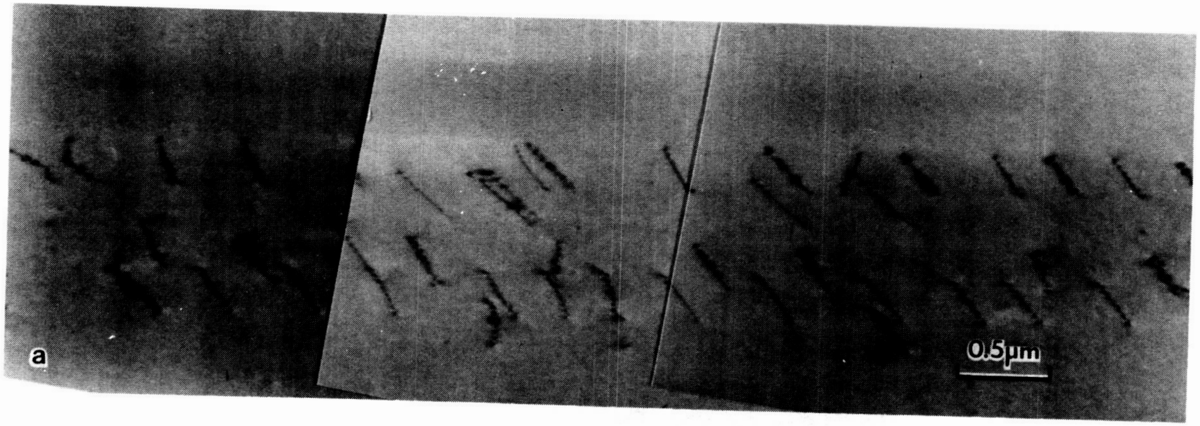

Twin Plane Tilted

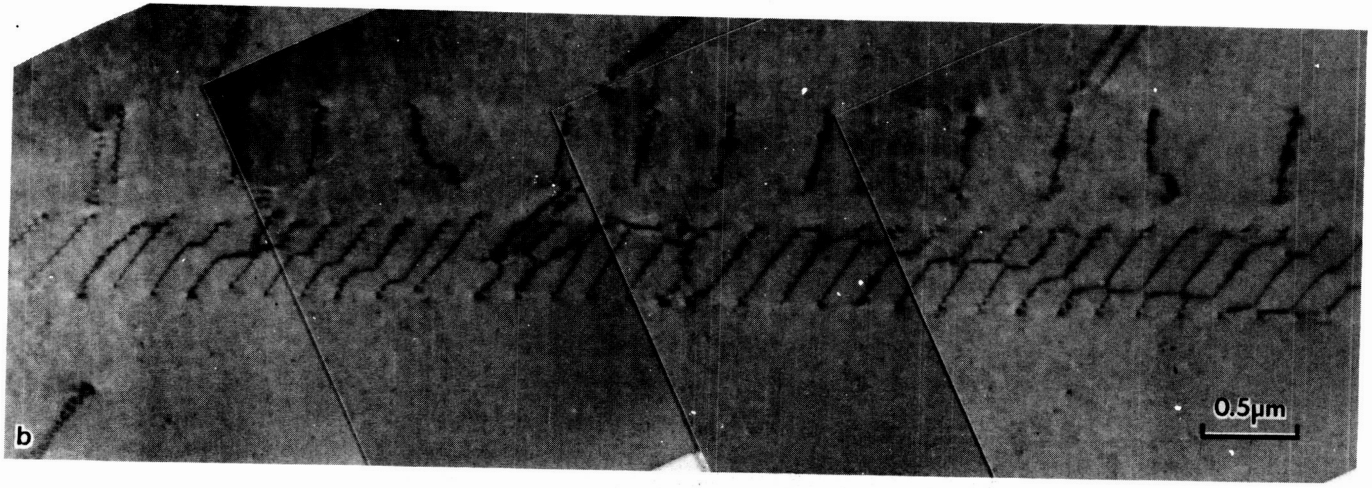

Figure 8. Cross-sectional TEM micrographs of cell 40C showing the formation of dislocation networks.

ORIGINAL PAGE IS
OF POOR QUALITY

ORIGINAL PAGE IS
OF POOR QUALITY

CELL 69A

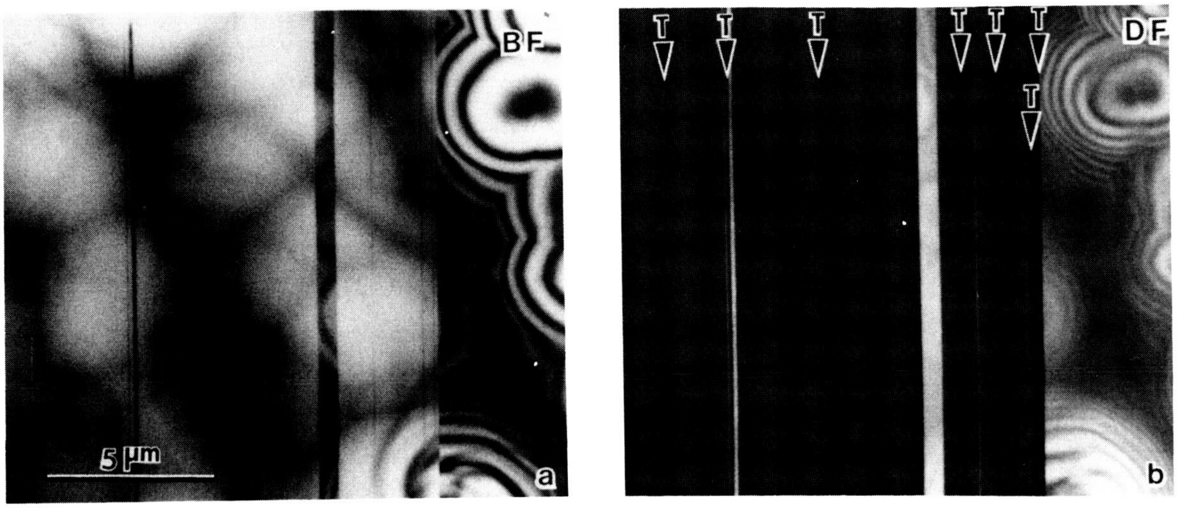

HIGH EFFICIENCY (14.3%)

Twin Plane Vertical

Figure 9. Cross-sectional TEM micrographs of cell 69A with the twin planes vertical.

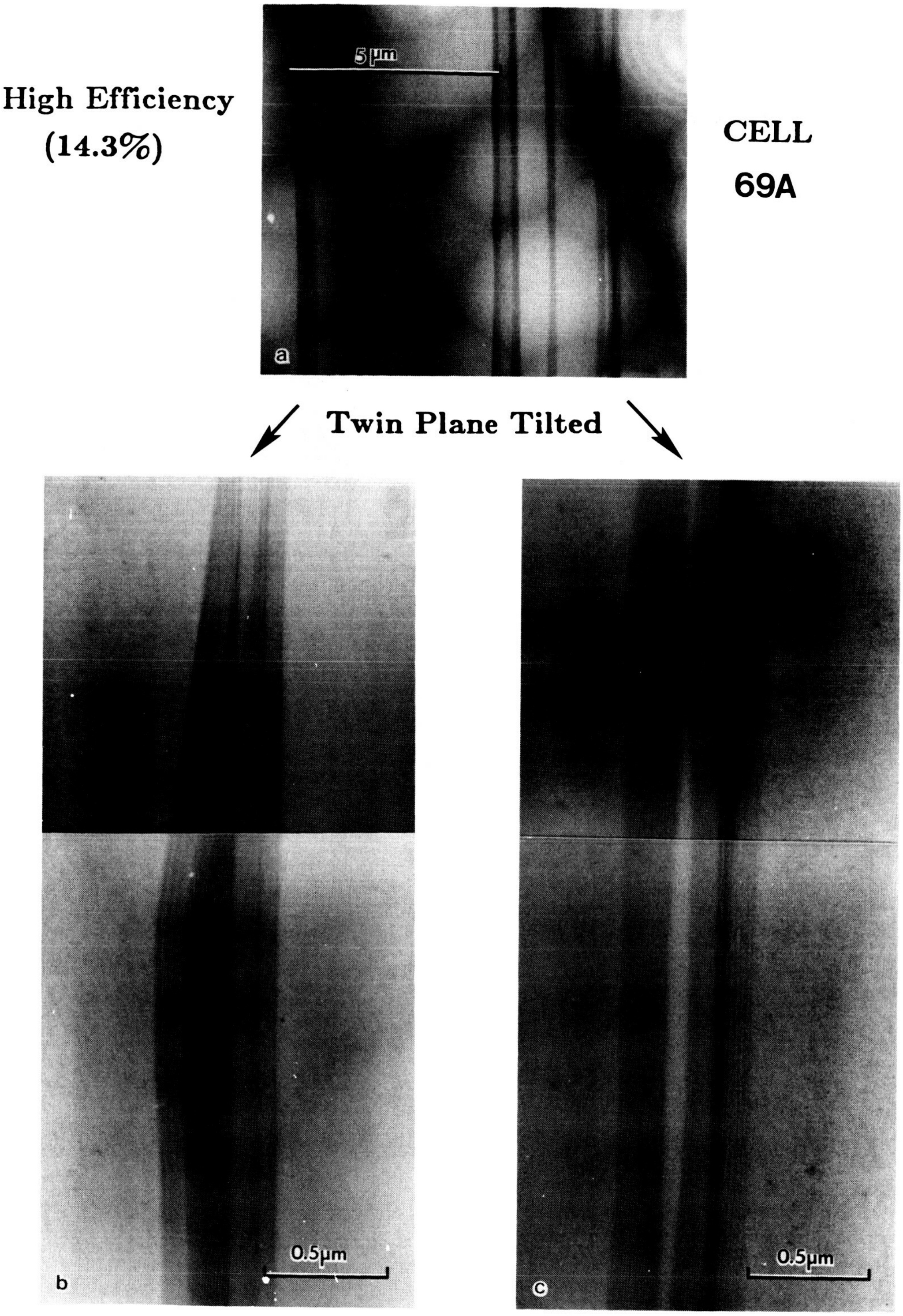

Figure 10. Cross-sectional TEM micrographs of cell 69A with the twin planes tilted.

CELL 17C: LOW EFFICIENCY (9.5%)

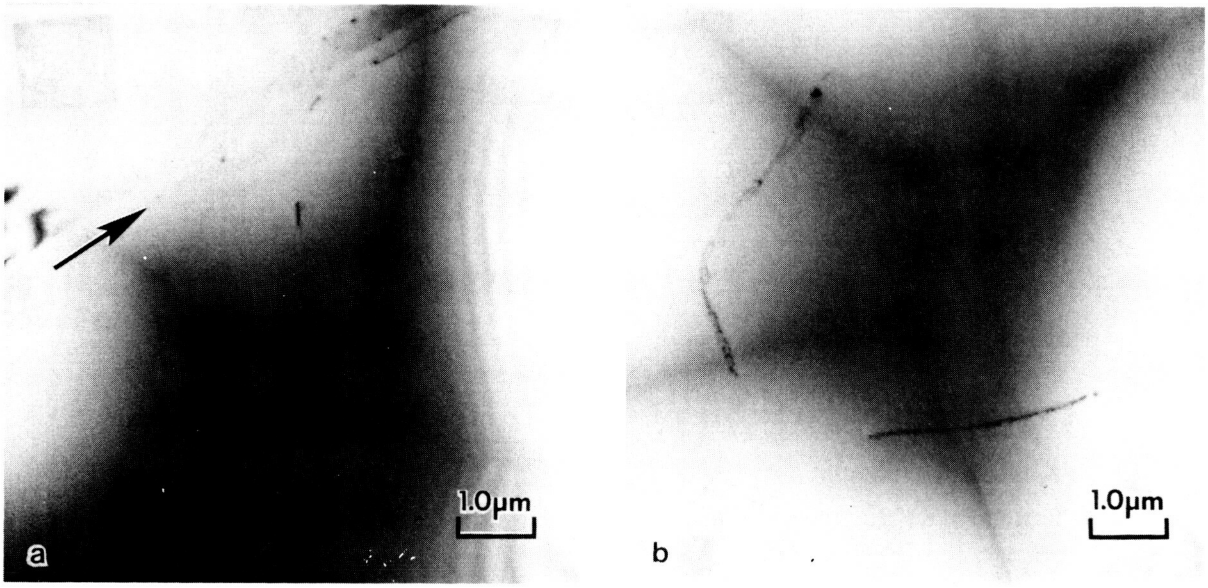

Bulk Si-Web Structure

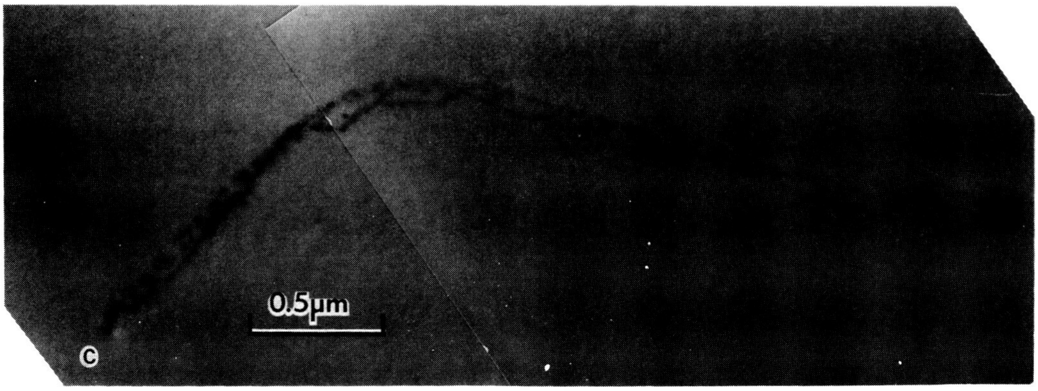

Figure 11. Cross-sectional TEM micrographs of cell 17C showing dislocation climb and the trail of precipitates left behind.

dislocation at its final location. The density of precipitates seems to be lowest at the final location and greatest at the initial location. These precipitates could be the result of impurities that were attached to the dislocation core, with the precipitates being deposited as the dislocation moved. The supply of impurities at the core would thereby be depleted, and the concentration of precipitates would decrease with the movement. It is also possible that the dislocation served as a nucleation site for impurities that were already present throughout the bulk, rather than being present only at the dislocation core.

The source and distribution of the impurities which form these precipitates and the identity of the precipitates are important factors which need to be understood if the electrical quality of the web material is to be improved. These factors are currently being investigated.

3.2 MODELLING THE HEAVILY TWINNED REGION

An examination of unprocessed web silicon and a number of web cells by cross-sectional TEM recently has shown that a heavily twinned region can be present inside the web ribbon. The width of this region is typically 6 μm, and within this region a large number (3 to 41 have been observed) of twin boundaries exist. In low-efficiency cells, this heavily twinned region also contains a large density of dislocations, many of which are decorated with impurity precipitates. Because of these dislocations and precipitates, the minority carrier diffusion length within this slab of highly defective material is quite low. By comparing the diffusion length, as measured by the surface photovoltage technique, with the average spacing between dislocations in the bulk, it has been concluded that the diffusion length is approximately equal to this average spacing of dislocations. The heavily twinned region exhibits a higher concentration of dislocations than the bulk, usually by a factor of 100. However, it should be pointed out that for high-efficiency baseline web cells (15%), the heavily twinned region contains very few dislocations ($< 10^4$ cm^{-2}). Such a cell would have a large diffusion length (>100 μm) associated with it, in spite of the large number of twin boundaries in the heavily twinned region.

An attempt was made to model the effect of the heavily twinned region on cell efficiency. A sketch of the cell structure that was assumed is given in Figure 12. The base thickness is taken to be 150 μm, with a 6 μm wide heavily twinned region located midway through the cell thickness. This region is assumed to have a diffusion length of 1 μm, which is the expected value for a dislocation density of 10^8 cm^{-2} within the region. Outside the heavily twinned region, in the remainder of the base, the diffusion length is taken as a parameter ranging from 10 μm to 300 μm. This is somewhat artificial, since the assumed high dislocation density in the heavily twinned region would normally imply a high dislocation density (perhaps 10^6 cm^{-2}) in the bulk. However, in order to focus on the effect of the heavily twinned region, this region was made to have a very low diffusion length, independent of the diffusion length of the remainder of the base.

The calculations were made using the modeling program SPCOLAY, provided by Professor Martin Wolf of the University of Pennsylvania. This one-dimensional numerical model is based upon a transformation of the minority carrier transport velocity.[1] The model treats the emitter and the base separately. The minority carrier transport velocities at the boundaries of the emitter and the base are represented by u_F, u_N and u'_F, u'_N in Figure 12.

The calculated values for Quantum Efficiency as a function of wavelength are shown in Figure 13, where the heavily twinned region is included, and in Figure 14, where the heavily twinned region is ignored. From Figure 13 it is seen that the heavily twinned region limits the effective cell thickness to the depth of this region (72 μm in this case), so that improving the diffusion length in the remainder of the base does not improve the cell performance. Without this heavily twinned region, the cell performance continues to improve with base diffusion length, as shown in Figure 14. By comparing Figures 13 and 14, it can be seen that the presence of the heavily twinned region is not important when the base diffusion length is considerably less (10

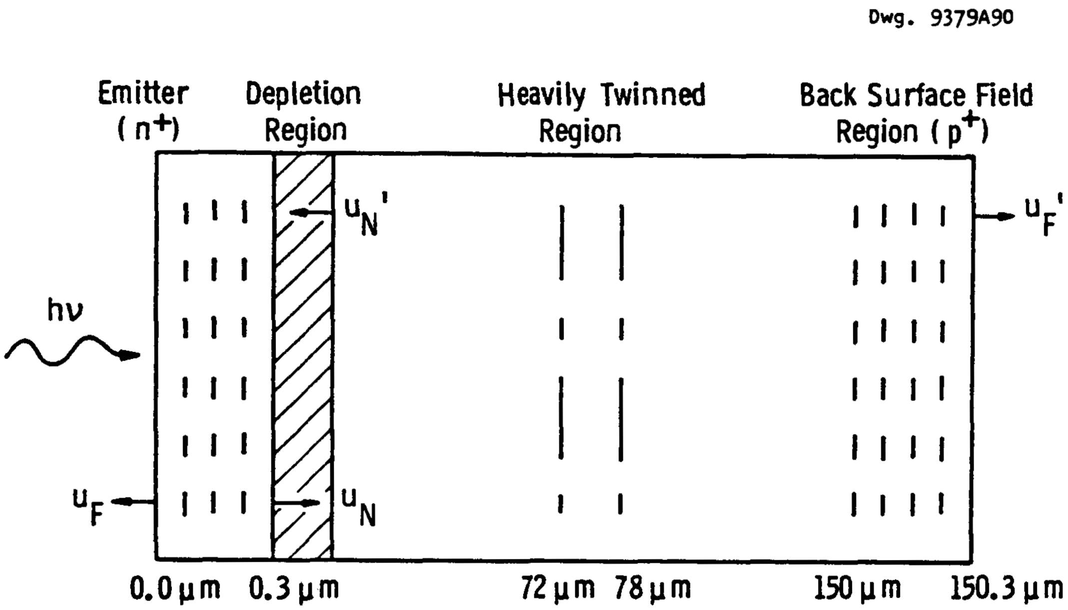

Assumptions:

1. Diffusion Length in Heavily-Twinned Region is 1 μm
2. Diffusion Length in Remainder of Base Varies Parametrically (10, 30, 60, 150, 300 μm)
3. $u_F = u_F' = 10^4$ cm/sec; $u_N = u_N' = 10^7$ cm/sec
4. Diffused Regions (n^+ and p^+) Divided into Four Subregions

Figure 12. Modeling the effect of the heavily twinned region on cell efficiency.

Curve 751285-A

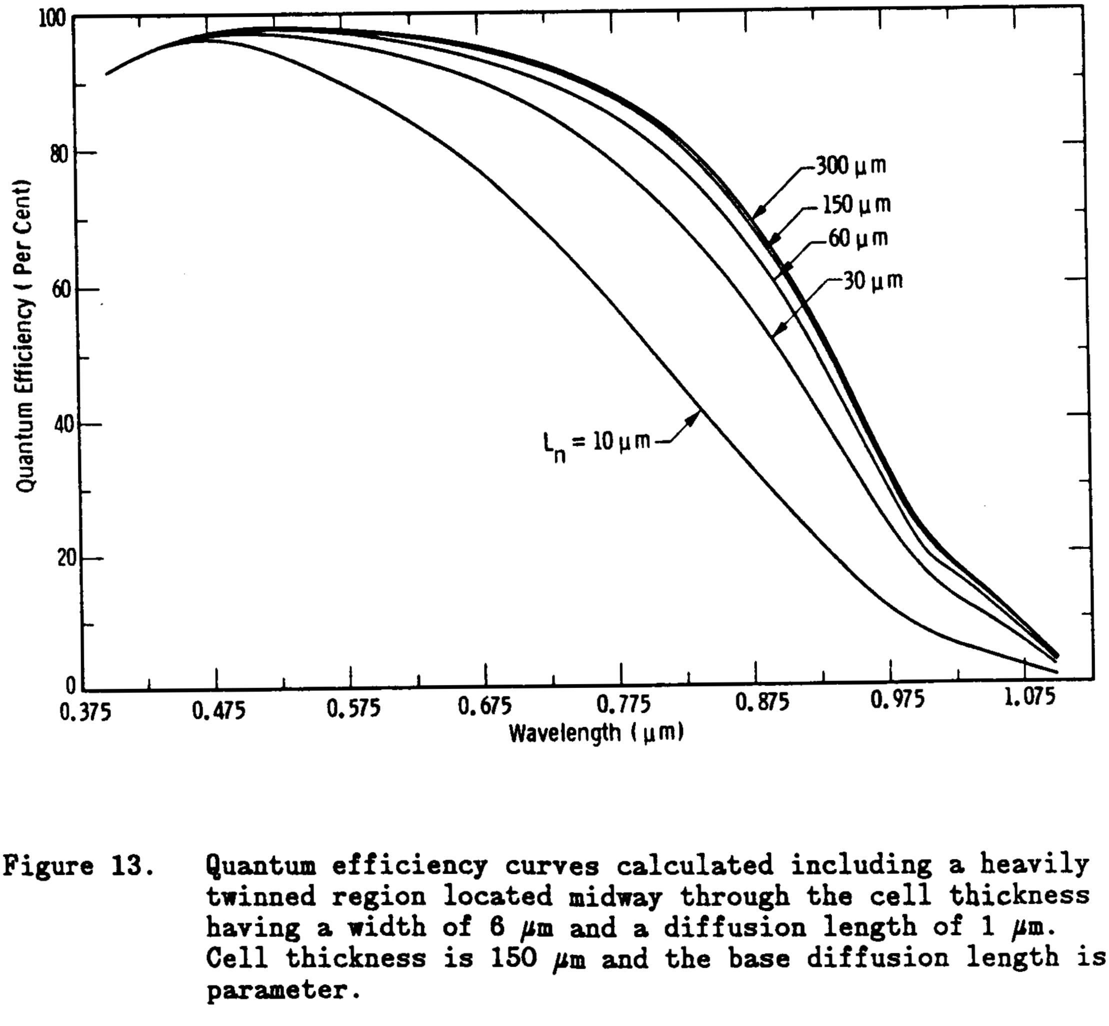

Figure 13. Quantum efficiency curves calculated including a heavily twinned region located midway through the cell thickness having a width of 6 μm and a diffusion length of 1 μm. Cell thickness is 150 μm and the base diffusion length is a parameter.

Curve 751284-A

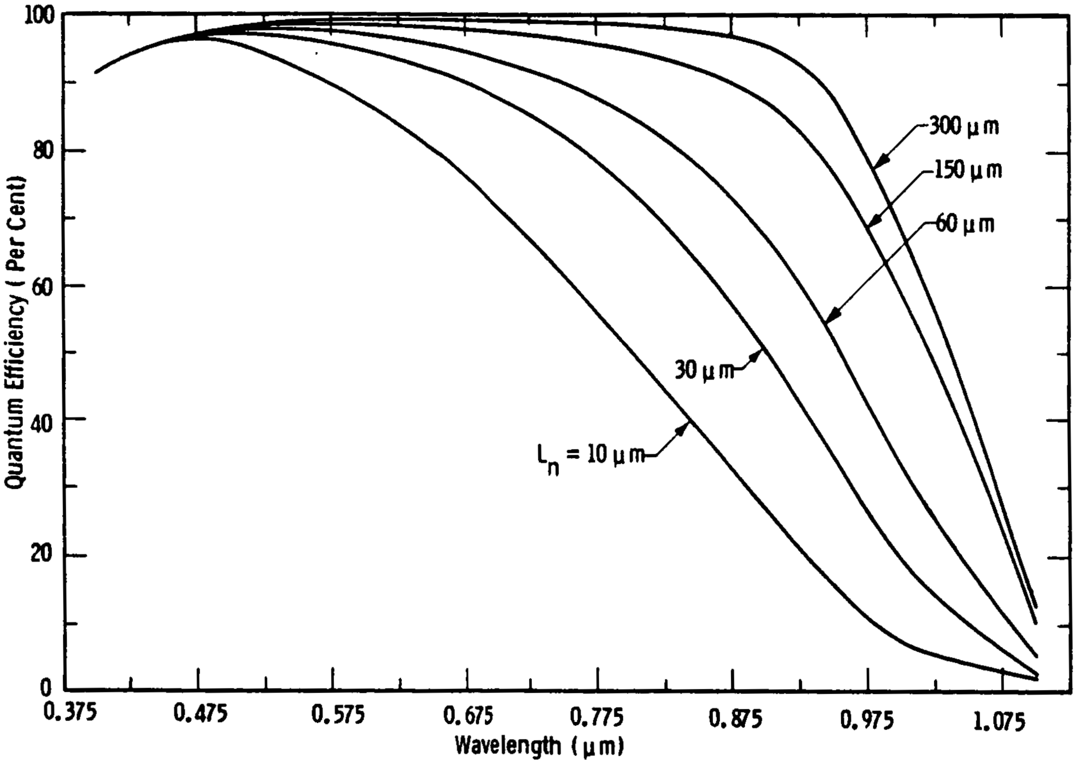

Figure 14. Quantum efficiency curves calculated ignoring heavily twinned region. Cell thickness is 150 μm and the base diffusion length is a parameter.

and 30 μm) than the depth of that region, as expected. When the base diffusion length exceeds (150 and 300 μm) that depth, then its presence is strongly felt.

The calculated cell parameters are given in Table 2. J_{ob} is the is the contribution to the reverse saturation current density from the base and J_e is the contribution from the emitter. Since only the base properties were changed in the calculations, J_{oe} is constant for all cases. Note from Table 2B that J_{ob} is limited to 41 pA/cm^2 by the heavily twinned region. Without this region, a cell efficiency of 17.0% is expected with a base diffussion length of 300 μm. With this region the cell efficiency is limited to 12.7%, even with a base diffusion length of 300 μm.

Web cells that have been examined by TEM and LBIC measurements are in good agreement with the calculated values shown in Table 2. The high efficiency baseline cells had L_n ~ 150 μm by SPV and efficiency ~ 15%. This agrees well with the 150 μm entry in Table 2A, and suggests that the heavily twinned region is electrically benign in such a cell, as indicated by the LBIC measurements reported earlier.[2] Conversely, the low-efficiency baseline cells had L_n ~ 20 μm by SPV and efficiency ~ 10%. This falls between the entries in Table 2B for 10 and 30 μm, as expected.

3.2.1 Hydrogen Ion Implantation Into Web Cells Using the Westinghouse System

In the previous quarterly progress report, the results of implanting web cells with hydrogen ions at Commonwealth Scientific Corporation in Alexandria, Virginia, were discussed. Since that time a system suitable for implanting hydrogen ions has been made available at the Westinghouse R&D Center. This system is a Veeco Microetch system, normally used with an argon ion beam for etching. A heated stage has been incorporated into the Westinghouse system to permit implantation into samples at temperatures up to 500°C. The implantation performed at Commonwealth Scientific did not affect the cells, and it was speculated that the temperature of the samples during the implant was too low, so

Table 2. Effect of Heavily Twinned Region on Cell Parameters

A. Neglecting Heavily Twinned Region

L_n (μm)	J_{ob} (pA/cm^2)	J_{sc} (mA/cm^2)	V_{oc} (V)	FF	η (%)	η' (%)
10	290	25.3	0.474	0.795	9.5	8.6
30	95	30.6	0.508	0.805	12.5	11.3
60	47	33.8	0.528	0.810	14.4	13.0
150	14	37.5	0.560	0.818	17.2	15.5
300	3.8	39.0	0.589	0.829	18.9	17.0

B. Including Heavily Twinned Region

L_n (μm)	J_{ob} (pA/cm^2)	J_{sc} (mA/cm^2)	V_{oc} (V)	FF	η (%)	η' (%)
10	290	25.3	0.474	0.795	9.5	8.6
30	98	30.3	0.507	0.805	12.4	11.1
60	58	32.1	0.522	0.809	13.5	12.2
150	43	32.8	0.530	0.810	14.1	12.6
300	41	32.9	0.531	0.827	14.2	12.7

Notes:

1. Calculations made using M. Wolf's program SPCOLAY.BAS
2. Base is boron-doped to 4 ohm-cm, 150 μm thick
3. Heavily twinned region taken to have a width of 6 μm and a diffusion length of 1 μm
4. J_{oe} = 1.6 pA/cm^2 in all cases
5. η' = 0.9 η to account for grid shadowing, light reflection, and resistive losses

that the hydrogen ions lacked the mobility to move to the defects to be passivated. The purpose of the heater, then, is to supply this additional thermal energy to the hydrogen ions in the sample. In addition, the implant energy at Commonwealth Scientific was 400 eV. In some of the work done with the Westinghouse system, the implant energy was increased to 1500 eV. At this higher energy, the sample is heated from the beam itself. No external heating was required, and improvements in cell efficiency were obtained, as discussed below.

The range of implantation parameters for the Westinghouse system are summarized in Table 3. Note that the beam is 4 inches in diameter. A schematic diagram for the Westinghouse system is given in Figure 15. In operation for hydrogen ion implantation, no voltage is applied to the electron suppressor grid and no current is supplied to the beam neutralizer filament. The current density for the ion beam is measured by a Faraday cup which simply allows a 1 cm^2 area of the beam to impinge on a shutter where the current is collected. During implantation the shutter is moved aside and the samples are exposed to the full 4-inch diameter beam.

Table 3. Implantation Parameters for the Hydrogen Ion Implanter at the Westinghouse R&D Center

Ion Energy:	300 - 1700 eV
Ion current density:	1 - 2 mA/cm^2
Ion beam diameter:	4 inches
Samples stage temperature:	$\lesssim$ 500°C

Figure 16 shows a photograph of the Veeco Microetch system at the Westinghouse R&D Center. The ion source is housed in the vertical cylindrical chamber in the upper right of the photograph. The hydrogen ion beam is directed downward toward the samples which are mounted horizontally on a molybdenum stage. Beneath the ion source are the

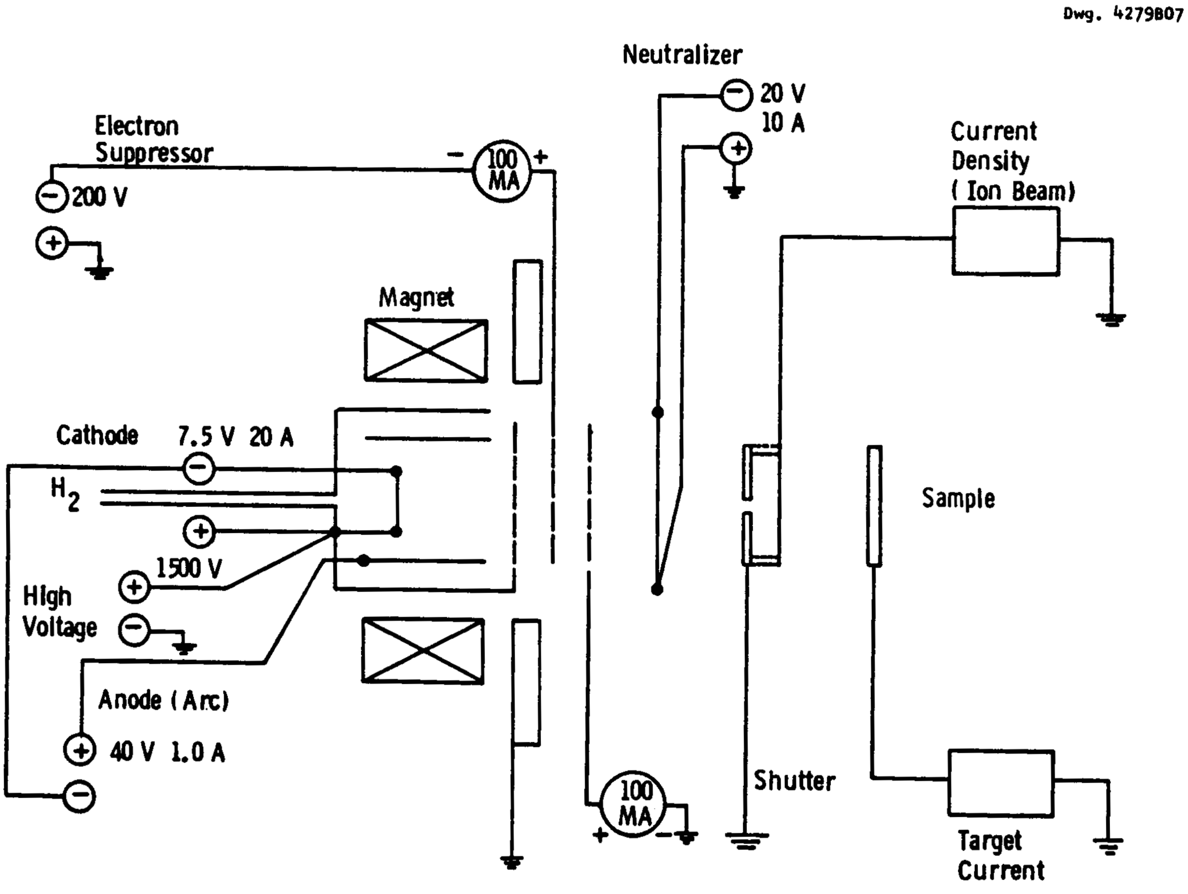

Figure 15. Schematic diagram of Veeco Microetch system adapted for low-energy, high-dose hydrogen ion implantation.

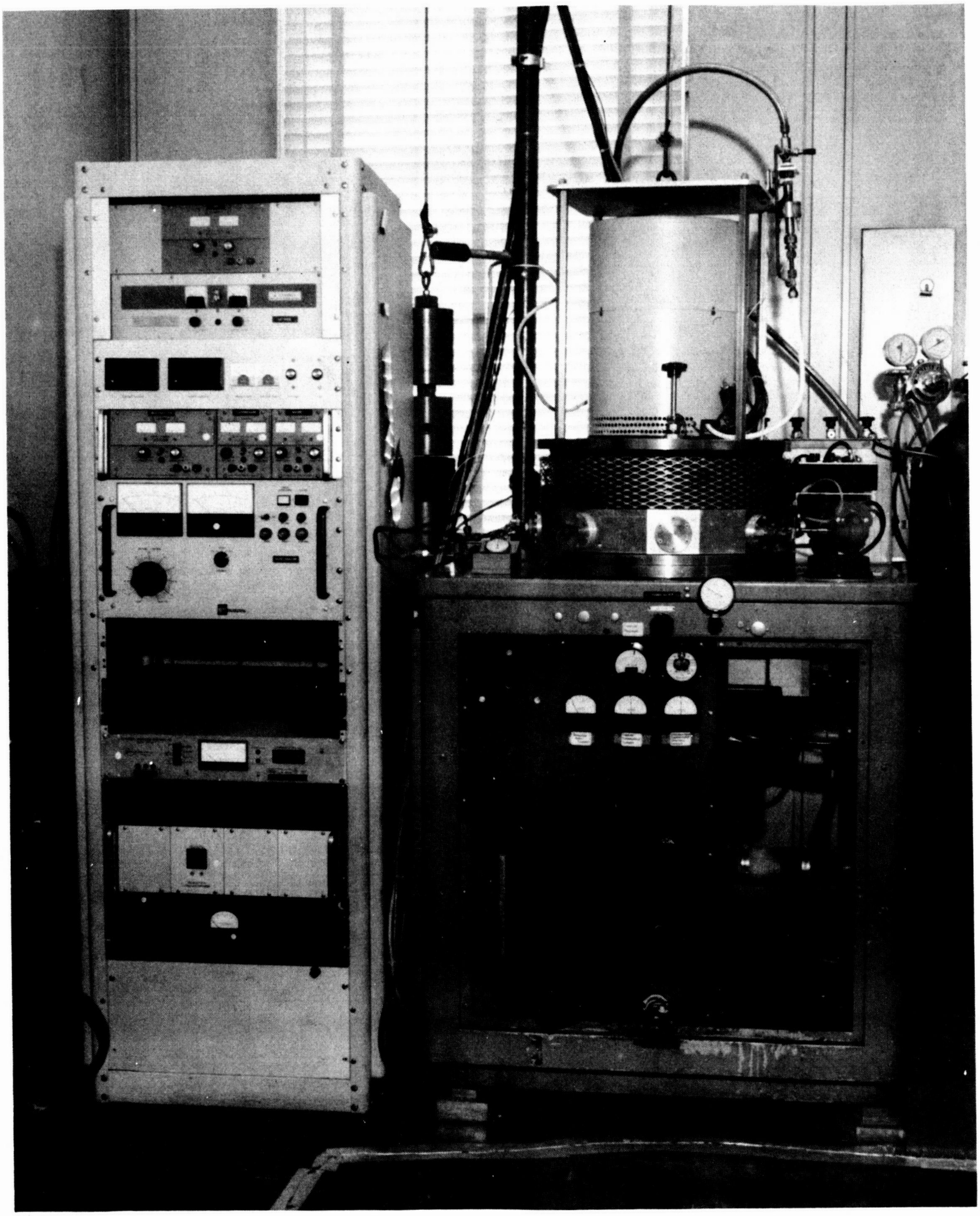

Figure 16. Photograph of the Veeco Microetch system which has been made available for hydrogen ion implantation at the Westinghouse R&D Center.

ORIGINAL PAGE IS
OF POOR QUALITY

vacuum system and gauges, and the power supplies and monitors are mounted in the electronics rack on the left. Figure 17 shows a sample being mounted on the stage. Figure 18 shows a web cell during hydrogen ion implantation. During implantation at 1500 eV, a violet glow is given off by the beam, and this light provided the illumination to expose the film for the photograph of Figure 18.

To date, only cells completed except for the antireflection coating have been implanted. Cell parameters and minority carrier diffusion length were measured before and after the implant for comparison. The choices of implant conditions (including stage temperature) are listed in Table 4 for the eight cells that have been implanted thus far. The effects of the implantation for these eight cells are summarized in Table 5. From Tables 4 and 5 it can be seen that implantation at 1500 eV and 2 mA/cm^2 for 2 minutes improved the efficiency and diffusion length of most cells. The best result was for cell 67-2, in which a cell efficiency of 8.0% (no AR) was increased to 9.8% by the implantation. The diffusion length for that sample also increased from 23 μm to 58 μm with the implantation. With an AR coating, the pre-implant efficiency would be expected to be 12.0% and the post-implant efficiency would then be 14.7%.

The implant time was also varied at 1500 eV. Sample X-2 was implanted at 2.0 mA/cm^2 for 8 minutes. Although J_{sc} increased with the implant, the efficiency decreased dramatically because of a decrease in the FF and V_{oc}. It is suspected that the cell temperature became excessive in this case and the metal comprising the grid lines then diffused into the silicon and shunted the junction. Cell 67-1 was implanted for only 0.5 minute at 1500 eV with 2 mA/cm^2 and showed no improvement. The preliminary conclusion is that no external substrate heating is required if the hydrogen ion beam energy is 1500 eV and the beam current density is 2 mA/cm^2. An implant time of 2 to 4 minutes is adequate, 8 minutes is excessive, and 0.5 minutes is insufficient.

Figure 17. Photograph of a web cell being mounted for hydrogen ion implantation.

ORIGINAL PAGE IS
OF POOR QUALITY

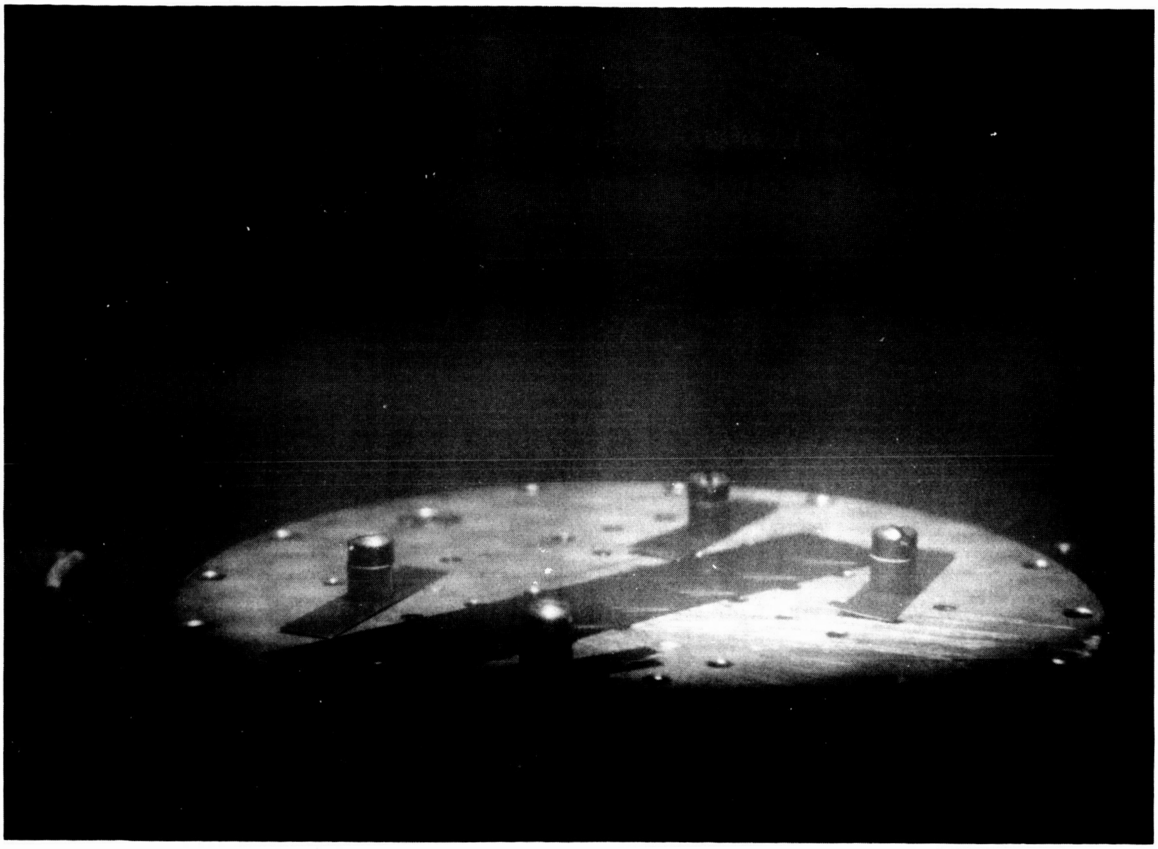

Figure 18. Photograph of web cell during hydrogen ion implantation (the light for exposing the photographic film came from a violet glow associated with the hydrogen ion beam).

Table 4. Conditions for H^+ Implantation into Web Cells

Cell	H^+ Energy (eV)	Current (Faraday Cup) (mA/cm^2)	Time (min)	Stage Temperature (°C)
63-1	400	1.0	4.0	300
63-2	1500	2.0	1.0	25
67-1	1500	2.0	0.5	25
67-2	1500	2.0	2.0	25
36-1	1500	2.0	2.0	25
36-2	1500	2.0	4.0	25
X-1	1500	2.0	2.0	25
X-2	1500	2.0	8.0	25

Notes:

1. Implantation was from front (emitter) side of cell
2. Cells had no anti-reflection coating and metallization system was evaporated Ti/Pd/Ag
3. Implantation done at Westinghouse R&D Center using a Veeco Microetch System with hydrogen
4. Pressure prior to introduction of hydrogen typically 5×10^{-6} torr.
5. With hydrogen input, pressure is regulated at 4×10^{-4} torr.
6. The H^+ beam was not neutralized.

Table 5. Effect of H^+ Implantation on Web Cell Parameters

Cell	Area (cm^2)	Condition	J_{sc} (mA/cm^2)	V_{oc} (V)	FF	η (%)	SPV L_n (μm)	QE L_n (μm)
63-1	4.0	pre-implant	20.2	0.520	0.782	8.22	-	-
		post-implant	20.4	0.520	0.776	8.22	-	-
63-2	4.0	pre-implant	20.6	0.524	0.775	8.39	34	-
		post-implant	21.6	0.526	0.769	8.73	36	-
67-1	4.0	pre-implant	20.4	0.508	0.779	8.05	23	-
		post-implant	19.5	0.507	0.753	7.44	23	21
67-2	4.0	pre-implant	20.5	0.508	0.768	8.00	23	-
		post-implant	23.7	0.554	0.745	9.78	58	49
36-1	4.0	pre-implant	18.4	0.511	0.777	7.30	23	-
		post-implant	20.6	0.525	0.756	8.16	75	-
36-2	4.0	pre-implant	20.4	0.511	0.762	7.93	26	-
		post-implant	22.7	0.524	0.749	8.92	94	-
X-1	1.0	pre-implant	20.3	0.583	0.788	9.31	44	-
		post-implant	21.1	0.574	0.769	9.33	57	-
X-2	1.0	pre-implant	20.2	0.581	0.789	9.26	39	-
		post-implant	22.1	0.489	0.484	5.23	43	-

Notes:

1. Measurement conditions: 100 mW/cm^2, AM1 spectrum, room temperature
2. Cells have no anti-reflection coating.
3. Web base material is boron-doped.
4. J_{sc} and V_{oc} increase while FF decreases with H+ implantation
5. L_n typically increases with H^+ implantation
6. At 1500 eV, stage heating does not seem necessary.
7. Cells were prepared in Run CELL-1 and implanted in Run HYIMP-10

Only one trial (cell 63-1) was made with substrate heating (300°C) at 400 eV implant energy. This choice gave no improvement. Because a period of time (perhaps 30 minutes) is required for the stage temperature to stabilize before the implant can be initiated, the use of external heating of the sample was not pursued further. The positive results obtained with a 1500 eV beam energy suggest that external stage heating may not be necessary if adequate self-heating of the sample is obtained from the beam alone.

Additional experiments with temperature-sensitive crayons will be conducted to determine the sample temperature at the end of the implantation period. Attempts will also be made to implant samples immediately after boron and phosphorus diffusions, before the metal grid lines are applied. This is an appropriate point in the process sequence to introduce hydrogen implantation. Cells fabricated with and without hydrogen implantation will be compared and the results will be evaluated.

3.3 CELL FABRICATION

It has been demonstrated that silicon web can be grown and processed with a dislocation density that is below the detecton limit of TEM, and that with such material it is possible to fabricate cells with efficiencies exceeding 15% by the baseline processing sequence at Westinghouse AESD. However, the growth conditions are not sufficiently well controlled as yet to produce, at will, web material in which the diffusion length approaches the thickness. Since such superior quality material is required in order to meet the efficiency objectives of this program, the material must be screened in some way before it receives processing beyond what is given in the baseline sequence. This screening can take one of two forms. The diffusion length can be measured immediately after the web has undergone both boron and phosphorus diffusions, and only those web strips which have an adequate diffusion length can be selected for enhanced processing. Alternatively, completed cells which have been processed at AESD and have been found to have superior efficiency ($\geq$ 15.5%) can be selected. The metal grid lines and the AR coating can then be stripped and enhanced processing (such as oxide passivation, the deposition of a double layer AR coating, and the reduction of the metal-to-silicon contact area in the grid system) can be employed. During this reporting period, the latter approach has been taken. Cell 61B with an efficiency of 15.5% (J_{sc} = 33.2 mA/cm^2, V_{oc} = 0.584 V, and FF = 0.79) after AESD baseline processing, was stripped and reprocessed. In addition, low-resistivity Wacker float-zone silicon, which had undergone boron and phosphorus diffusions at the Westinghouse R&D Center, was also processed along with additional web material. Web cells having an area of 4 cm^2, as required by this program, were fabricated for the first time. Cells were fabricated both with and without an oxide passivation of the external surfaces.

3.3.1 Web and Float-Zone Cells Without Oxide Passivation

Lighted I-V data for cells made with web material (93 and 79), Wacker float-zone silicon (FZQ1), and with a web cell which had been stripped and reprocessed (61B) are given in Table 6. Part a of the table gives the data before the AR coating, with only the aluminum back-surface reflector in place. Part b of the table gives the data after an evaporated double-layer antireflection (AR) coating, consisting of 600 Å of ZnS and 1000 Å of MgF_2, was applied. Also listed are the values of diffusion length, as measured by the surface photovoltage (SPV) technique and the thickness of the cells. Note that efficiencies as high as 17.3% have been measured for web cell 61B-3. This is attributed to the large value of diffusion length (160 μm) which approaches the cell thickness (190 μm), and to the significant enchancement in short-circuit current (50%) and efficiency (54%) associated with the double-layer AR coating. The short circuit current density for web cell 61B-3 (38.2 mA/cm) is measured to be larger even than that of float-zone cell FZQ1-1 (36.2 mA/cm2). This is a result of two factors. First, the thickness of the two cells is different (190 μm and 375 μm) so that the aluminum back-surface reflector is more

Table 6. Lighted I-V and Diffusion Length Data for Web and Float-Zone Silicon Cells Before and After Double-Layer Antireflection Coating. (Run Cell-1)

Cell ID	Processing Run	Crystal ID	Area (cm^2)	J_{sc} (mA/cm^2)	V_{oc} (V)	FF	η (%)	SPV L_n (µm)	Thickness (µm)
a) Before AR Coating									
93-2	4N04-73W	-	4.0	21.6	0.503	0.760	8.26	-	146
79-1	4N04-73W	-	4.0	22.9	0.542	0.781	9.70	49	152
61B-1	0909-49E	0-006-3.4	1.0	25.2	0.565	0.776	11.1	110	190
61B-2	0909-49E	0-006-3.4	1.0	25.3	0.564	0.776	11.1	150	190
61B-3	0909-49E	0-006-3.4	1.0	25.4	0.565	0.776	11.2	170	190
FZQ1-1	R&D Diffusion	Float Zone	1.0	24.6	0.600	0.813	12.0	~200	375
FZQ1-6	R&D Diffusion	Float Zone	4.0	24.6	0.587	0.746	10.8	~200	375
b) After AR Coating (600 Å ZnS + 1000 Å MgF_2 on bare Si)									
93-2	4N04-73W	-	4.0	32.1	0.533	0.758	13.0	-	146
79-1	4N04-73W	-	4.0	34.1	0.559	0.782	14.9	-	152
61B-1	0909-49E	0-006-3.4	1.0	38.0	0.586	0.774	17.2	110	190
61B-2	0909-49E	0-006-3.4	1.0	38.1	0.586	0.772	17.2	120	190
61B-3	0909-49E	0-006-3.4	1.0	38.2	0.586	0.773	17.3	160	190
FZQ1-1	R&D Diffusion	Float Zone	1.0	36.2	0.607	0.803	17.7	-	375
FZQ1-6	R&D Diffusion	Float Zone	4.0	36.4	0.598	0.736	16.0	-	375

Notes:
1) Cells have 1000 Å evaporated aluminum back-surface reflector.
2) Evaporated layers of 600 Å ZnS and 1000 Å MgF_2 comprise the AR coating on bare (unpassivated) silicon.
3) Test Conditions: AM1 spectrum (tungsten-halogen ELH lamp), 100 mW/cm^2, room temperature.
4) Web cells have a boron-doped base with 4 ohm-cm nominal resistivity.
Float-Zone (Wacker) cells have a boron-doped base with 0.2 ohm-cm nominal resistivity.

effective for the thinner web cell than for the float-zone cell. Second, the AR coatings for the two cells were deposited at two different times, and the web cell received a greater enhancement in short-circuit current (50%) than did the float-zone cell (47%). The enhancement of various cell parameters because of the AR coating is given in Table 7. The dark I-V parameters for the three cells in strip 61B are given in Table 8.

This efficiency of 17.3% represents a new high for web cells. The previous high was 16.9%, which was also measured in the same way for a 1 cm^2 cell in which the area was defined similarly by a mesa etch. Cell 61B-3 was also measured at the Jet Propulsion Laboratory.[3] The values obtained at JPL were 34.2 mA/cm^2 (J_{sc}), 0.592V (V_{oc}), 0.790 (FF), and 16.0% (η); the corresponding values obtained at the Westinghouse R&D Center (Table 6b) are 38.2 mA/cm^2, 0.586 V, 0.773, and 17.3%, respectively. The significant difference in efficiency (16.0% and 17.3%) reflects the fact that the calibration standard at JPL was changed during the course of this program. The new standard gives efficiency measurements that are approximately 7% (relative) lower than measurements based on the previous standard. The Westinghouse measurements are based on the previous standard, which was in effect at the beginning of this program. Since the original contract goals were written when the previous standard was in effect, Westinghouse will continue to base its measurements for this program on the previous standard. It is clear, however, that an advance in the efficiency of web cells has been made.

Several additional measurements were made for cell 61B-3, which had the highest efficiency. The reflectivity is given in Figure 19. Note that it is low (minimum of 2%) and flat over much of the spectrum. Note also that the reflectivity rises dramatically for wavelengths above 0.98 μm. This is partly a consequence of the aluminum back-surface reflector, indicating that it is effective in providing a second pass through the silicon of some of the long-wavelength photons.

The measured internal quantum efficiency for cell 61B-3 is given in Figure 20. The quantum efficiency data at long wavelengths are

Table 7. Ratio of Cell Parameters After AR Coating to Cell Parameters Before AR Coating (Run Cell-1)

Cell ID	J_{sc}	V_{oc}	FF	η
93-2	1.49	1.06	1.00	1.57
79-1	1.49	1.03	1.00	1.54
61B-1	1.51	1.04	1.00	1.55
61B-2	1.51	1.04	0.99	1.55
61B-3	1.50	1.04	1.00	1.54
FZQ1-1	1.47	1.01	0.99	1.48
FZQ1-6	1.48	1.02	0.99	1.48

Notes: 1) Evaporated layers of 600 Å ZnS and 1000 Å MgF_2 comprise the AR coating on bare (unpassivated) silicon.

2) Data from Table 6 used to construct this table.

Table 8. Dark I-V Parameters for High-Efficiency Web Cells (Run Cell-1)

Cell ID	Area (cm^2)	J_{01} (A/cm^2)	J_{02} (A/cm^2)	N	R_{series} (ohm-cm^2)	R_{shunt} (kohm-cm^2)
61B-1	1.0	3.2×10^{-12}	2.3×10^{-7}	2.45	0.62	300
61B-2	1.0	2.6×10^{-12}	0.17×10^{-7}	1.77	0.52	3300
61B-3	1.0	3.4×10^{-12}	5.5×10^{-7}	2.87	0.59	110

Notes: 1) Dark I-V data are fitted to a function of the form:

$$J(V) = J_{01}\exp^{qV/kT} + J_{02}\exp^{qV/NkT}$$

2) Boron doping in base is 2.0×10^{15} cm^{-3} (6.3 ohm-cm)

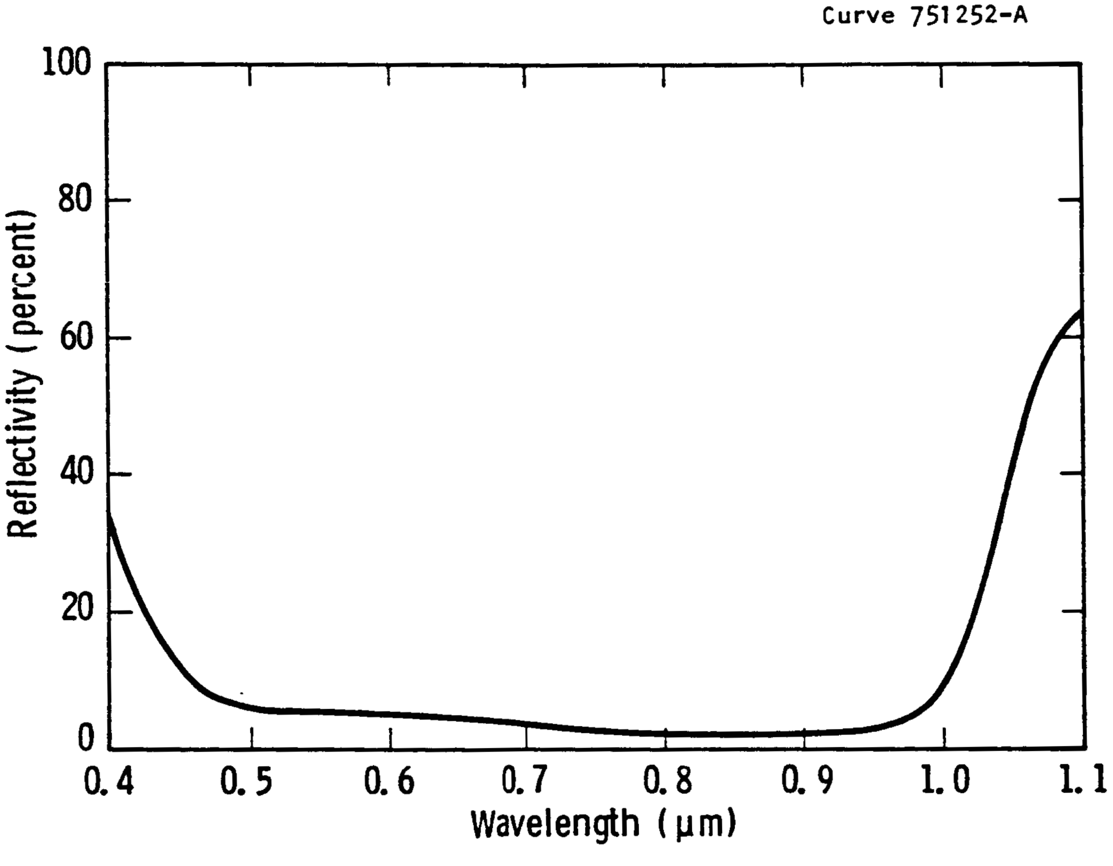

Figure 19. Measured reflectivity for web cell 61B-3 after the deposition of the antireflection coating (600 Å ZnS and 1000 Å MgF_2) on bare (unpassivated) silicon. The cell has a 1000 Å evaporated aluminum back-surface reflector. (Run Cell-1)

Curve 751253-A

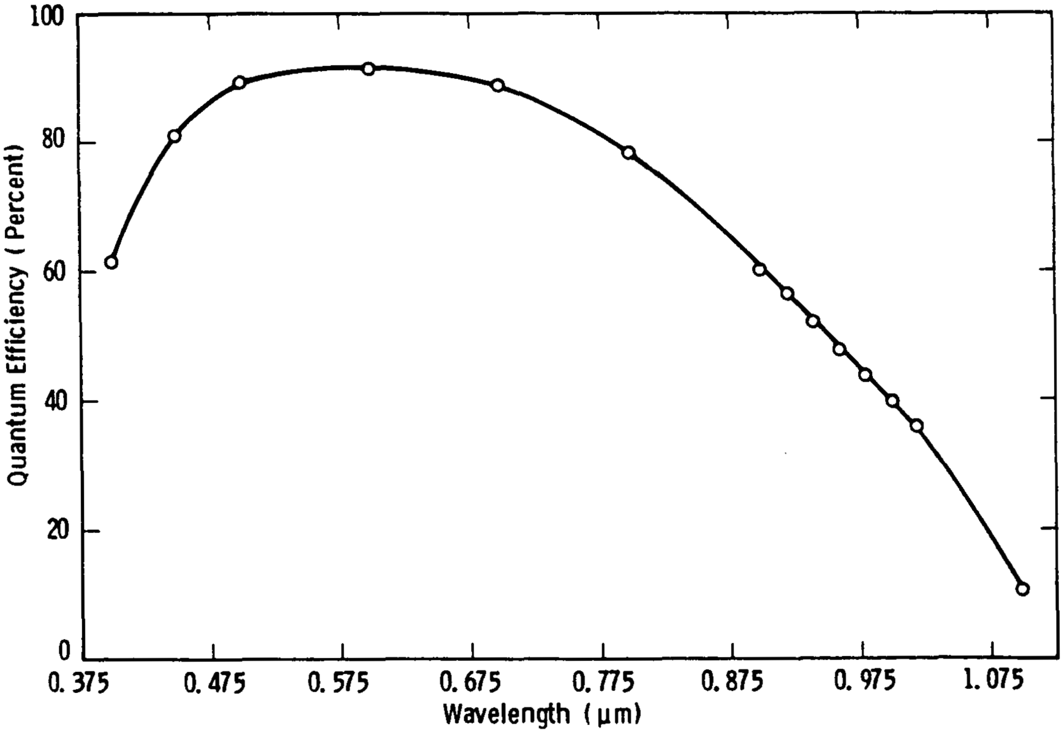

Figure 20. Measured quantum efficiency for web cell 61B-3 after the deposition of the antireflection coating (600 Å ZnS and 1000 Å MgF_2) on bare (unpassivated) silicon. The cell has a 1000 Å evaporated aluminum back-surface reflector. (Run Cell-1)

normally used to determine the diffusion length in the base of the cell. A plot of this type for cell 61B-3 is given in Figure 21. When the diffusion length is less than one-half the thickness of the cell, such a plot yields a straight line, where the slope of the line is equal to the diffusion length. However, the slope of the line in Figure 21 is continually changing in a way that suggests that the effective diffusion length increases with wavelength. This indicates that the back surface reflector is effective in this cell, and reinforces the contention that the large short-circuit current for this cell is partly attributed to the back-surface reflector.

The dopant profiles for the front and back junctions of partial cell 61B-4 (adjacent to cell 61B-3), as determined by spreading resistance measurements, are given in Figures 22 and 23. Note from Figure 22 that the junction is relatively shallow (0.26 μm), the surface concentration is low (5.7 x 10^{19} cm^{-3}), and the doping concentration decreases rapidly from the front surface. This rapid decrease results in a drift field built into the emitter which acts to keep the minority carriers (holes) away from the front surface. This effect, along with the relatively low surface concentration and shallow junction, may explain why the internal quantum efficiency at 400 nm is a respectable 60% in spite of the absence of a passivating oxide.

3.3.2 Web and Float-Zone Cells With Oxide Passivation

Some cells were also fabricated in which the front and back surfaces were passivated with a thin (~ 100 Å) oxide grown at 800°C for 5 minutes. The front oxide thicknesses ranged from 73 Å to 143 Å for 11 samples, as determined by ellipsometer measurements. Contact to the back was made using the same grid line pattern that was used for the front. The process sequence for cells with front and back surfaces passivated with thermal SiO_2 is outlined in Figure 24. Lighted I-V data for some of the cells are given in Table 9. Comparing some entries in Table 9a with those in Table 6a, particularly 79P with 79 and FZP3 with FZQ1, suggests that the passivation has improved the open-circuit voltage by perhaps 10 mV. However, the double-layer AR coating did not

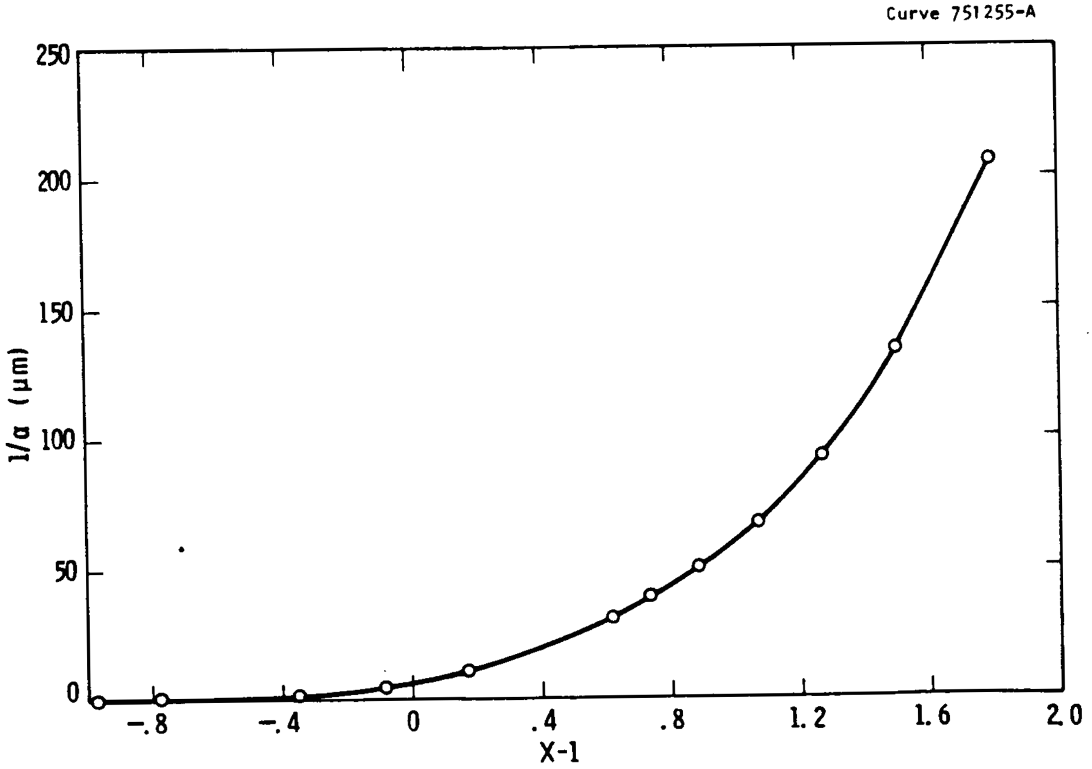

Figure 21. Diffusion length plot constructed from quantum efficiency data for web cell 61B-3 showing the effective increase in minority carrier diffusion length with wavelength. (Run Cell-1).

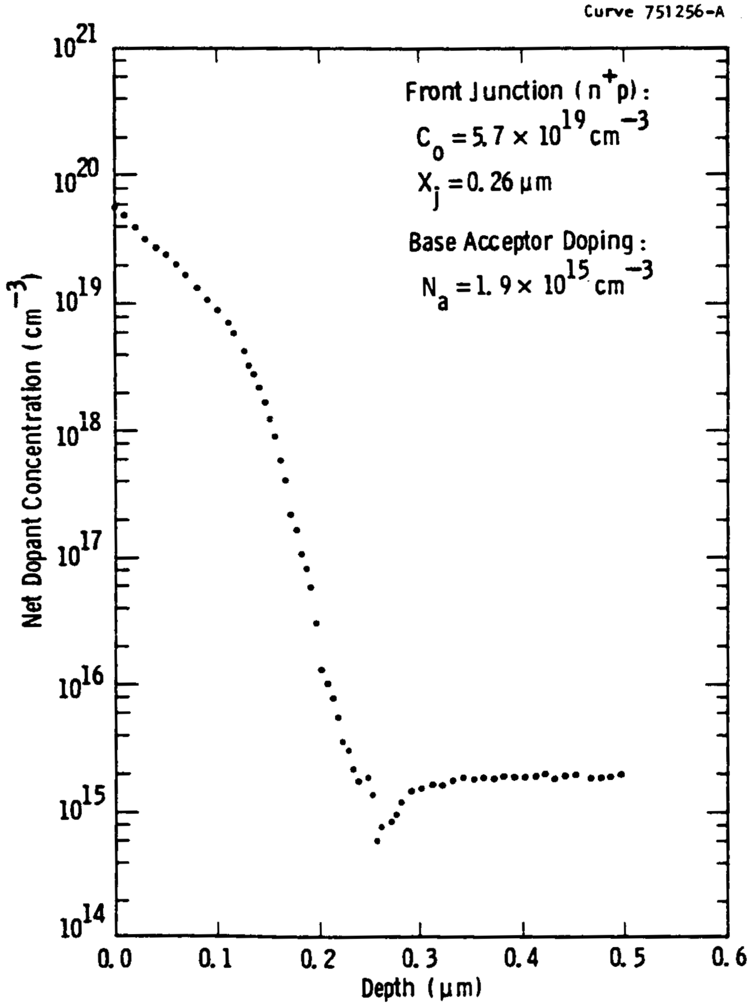

Figure 22. Dopant profile for the front (n^+p) junction of partial web cell 61B-4 by spreading resistance. (Run Cell-1).

Curve 751254-A

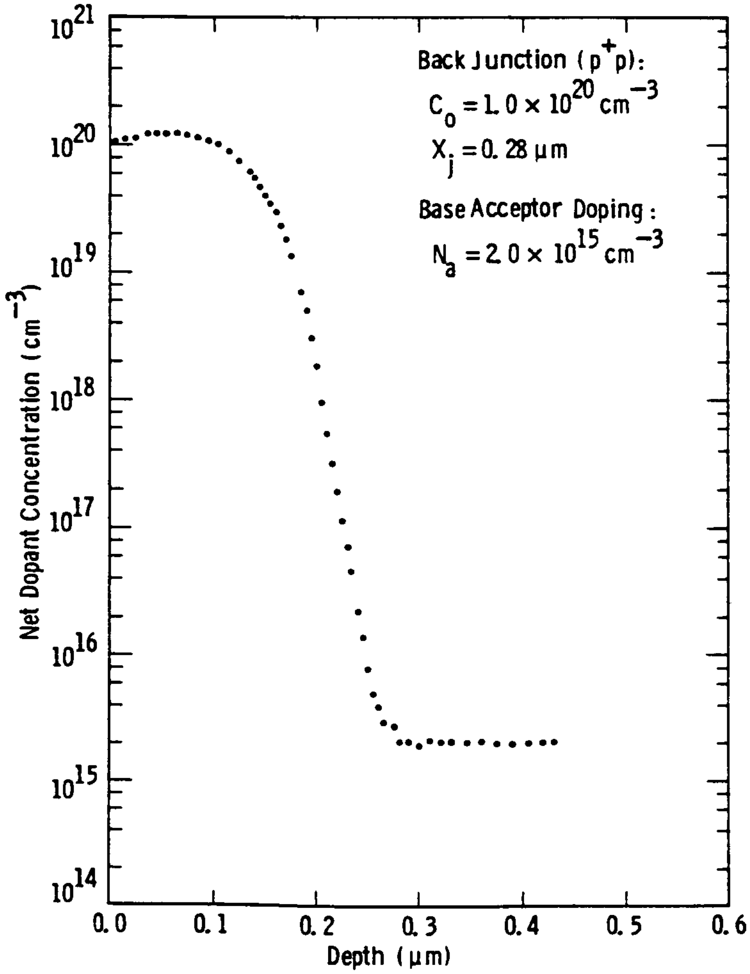

Figure 23. Dopant profile for the back (p^+p) region of partial web cell 61B-4 by spreading resistance. (Run Cell-1).

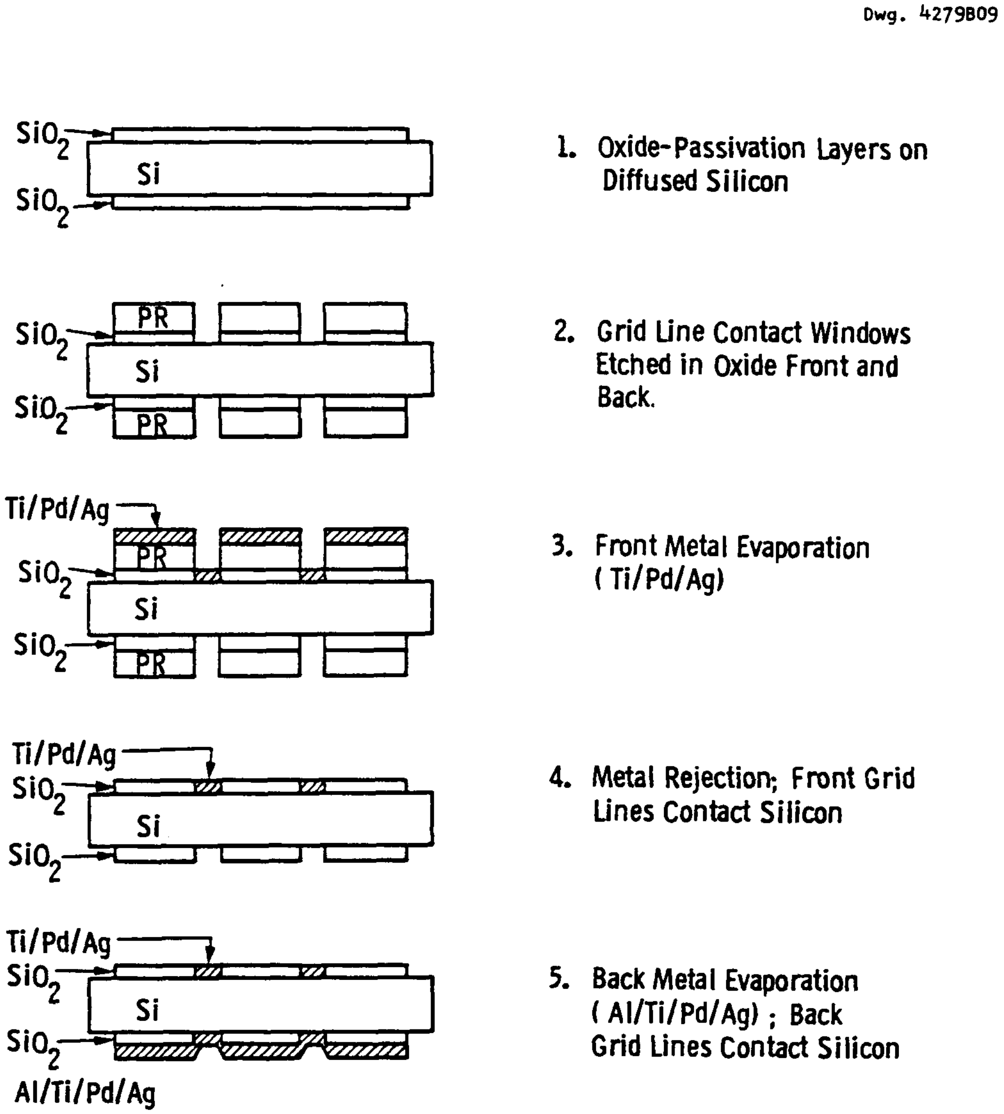

Figure 24. Process sequence for metal contact to silicon along grid line openings in oxide.

Table 9. Lighted I-V Data for Oxide-Passivated Web and Float-Zone Silicon Cells Before and After Double-Layer Antireflection Coating. (Run Cell-1)

a) Before AR coating, but after oxide (~ 100 Å) passivation front and back with sintering.

Cell ID	Processing Run	Crystal ID	Area (cm^2)	J_{sc} (mA/cm^2)	V_{oc} (V)	FF	η (%)
38BP-2*	L5113-01	7-284/285	4.0	20.8	0.587	0.805	9.81
79P-2	4N04-73W	-	4.0	22.9	0.553	0.792	10.0
61BP-2	0909-49E	0-006-3.4	4.0	24.1	0.553	0.775	10.3
FZP3-4*	R&D Diffusion	Float Zone	1.0	24.1	0.613	0.810	12.0
FZP3-8*	R&D Diffusion	Float Zone	4.0	23.7	0.608	0.811	11.7

b) After AR Coating (430 Å ZnS + 1000 Å MgF_2 on 100 Å SiO_2)

Cell ID	Processing Run	Crystal ID	Area (cm^2)	J_{sc} (mA/cm^2)	V_{oc} (V)	FF	η (%)
38BP-2*	L5113-01	7-284/285	4.0	29.3	0.596	0.795	13.9
79P-2	4N04-73W	-	4.0	33.4	0.564	0.774	14.6
61BP-2	0909-49E	0-006-3.4	4.0	35.3	0.565	0.753	15.0
FZP3-4*	R&D Diffusion	Float Zone	1.0	34.7	0.612	0.798	17.2
FZP3-8*	R&D Diffusion	Float Zone	4.0	34.1	0.619	0.791	16.7

* ~ 0.2 ohm-cm, boron doped.

increase the short-circuit current as significantly as it did for the unpassivated cells of Table 6. This indicates that a nonoptimum thickness of ZnS may have been used in this case, and that the effect of the passivating oxide was not taken into account properly.

A portion of the original cell 61B was processed in this group and is listed in Table 9 as 61BP-2. It appears that the oxide passivation may have degraded this sample somewhat, perhaps because of some residual metal which may have remained after the original grid lines were removed by etching. The highest efficiency obtained for a passivated web cell was 15.0%, and the highest for a float-zone cell was 17.2%.

3.4 DESIGN OF A GRID SYSTEM WITH REDUCED METAL/SILICON CONTACT AREA

The contact between metal and silicon is a region of high recombination in which the influence of the metal is felt beyond the area covered by the metal itself. Therefore, it is desirable to reduce this contact area to as low a value as possible. A mask was designed in which the metal/silicon contact area is reduced by a factor of 40 compared to the present design. This is achieved by having the grid lines contact the silicon only at regularly spaced intervals of 800 µm. The contact area is a square having the dimension of the width of the grid line, which is typically 20 µm. The remaining length of the grid line is located on top of the passivating oxide.

This is expected to reduce the recombination in the vicinity of the metal/silicon interface, and therefore to increase the short-circuit current and open-circuit voltage, especially for cells with a low-resistivity (0.2 ohm-cm) base. Calculations of the contribution of the contact resistance to the total series resistance indicate that this reduction will not degrade the series resistance, provided the doping concentration at the silicon surface exceeds 10^{19} cm^{-3}. The proposed process sequence for cells in which metal contact is made to the silicon only at dot openings in the passivating oxide is shown in Figure 25.

Dwg. 4279B08

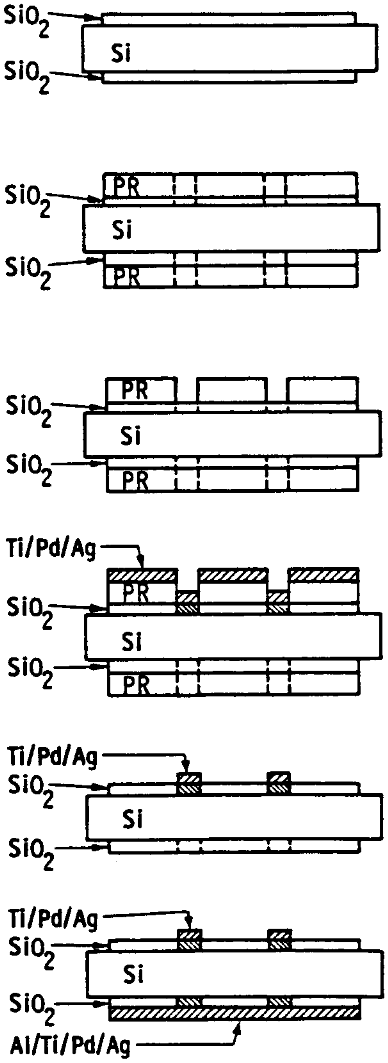

1. Oxide-Passivation Layers on Diffused Silicon
2. Dot Contact Windows Etched in Oxide on Front and Back (Mask 1)
3. Photoresist Removed for Grid Line on Front (Mask 2)
4. Front Metal Evaporation (Ti/Pd/Ag)
5. Metal Rejection; Grid Line on Oxide Except for Dot Contact to Silicon
6. Back Metal Evaporation (Al/Ti/Pd/Ag); Contact to Silicon Made Only at Dots

Figure 25. Processs sequence for metal contact to silicon at dot openings in oxide only.

3.5 VERIFICATION OF DLTS MEASUREMENT TECHNIQUE FOR BEVELED SAMPLES

As discussed in the previous quarterly progress report for this program, the beveling of silicon samples with Syton was found to introduce a spurious deep level in the DLTS measurements. It was, therefore, thought to be important to demonstrate that the DLTS measurement for stripes on beveled samples does yield accurate results, provided the beveling damage is removed by etching. This was demonstrated using a wafer cut from a Czochralski (CZ) ingot which was boron-doped to 4 ohm-cm and which had titanium grown into the ingot from the melt (ingot 210-Ti). The titanium concentration and energy level in this sample were known from previous DLTS measurements using conventional Schottky diodes in the form of dots on the wafer surface.

A beveled sample, (2 x 5) mm in size, was prepared from this wafer with the standard 2° 52' bevel angle. Schottky diodes in the form of stripes 150 μm wide, 1500 μm long, with 50 μm spacing, were formed on the beveled and on the unbeveled surfaces. The Schottky metal was 150 Å Ti, with 400 Å Au deposited on top of the Ti to facilitate wire bonding. The depletion layer capacitance of such a Schottky diode under a reverse bias of 6 volts was 11.7 pF. A DLTS scan for a stripe of the beveled surface is given in Figure 26. The concentration of titanium (N_{Ti}) was 2.2×10^{-13} cm^3, and the energy level was $E_v + 0.31$ eV. These values agree reasonably well with those determined previously using the conventional Schottky diodes: $N_{Ti} = 2.9 \times 10^{13}$ cm^{-3} and $E_{Ti} = E_v + 0.30$ eV.[4]

Note from Figure 26 that the DLTS peak is of normal width, even though the metal stripe was deposited on the beveled surface. This is different from results observed earlier in which the titanium peak for the same material was considerably broadened by the surface damage. Similar results were obtained for another stripe on the beveled surface and for a stripe on the unbeveled surface. This indicates that the Sirtl etching has been effective in removing surface damage and that DLTS measurements, which are free from artifacts of sample preparation, can be made with beveled samples.

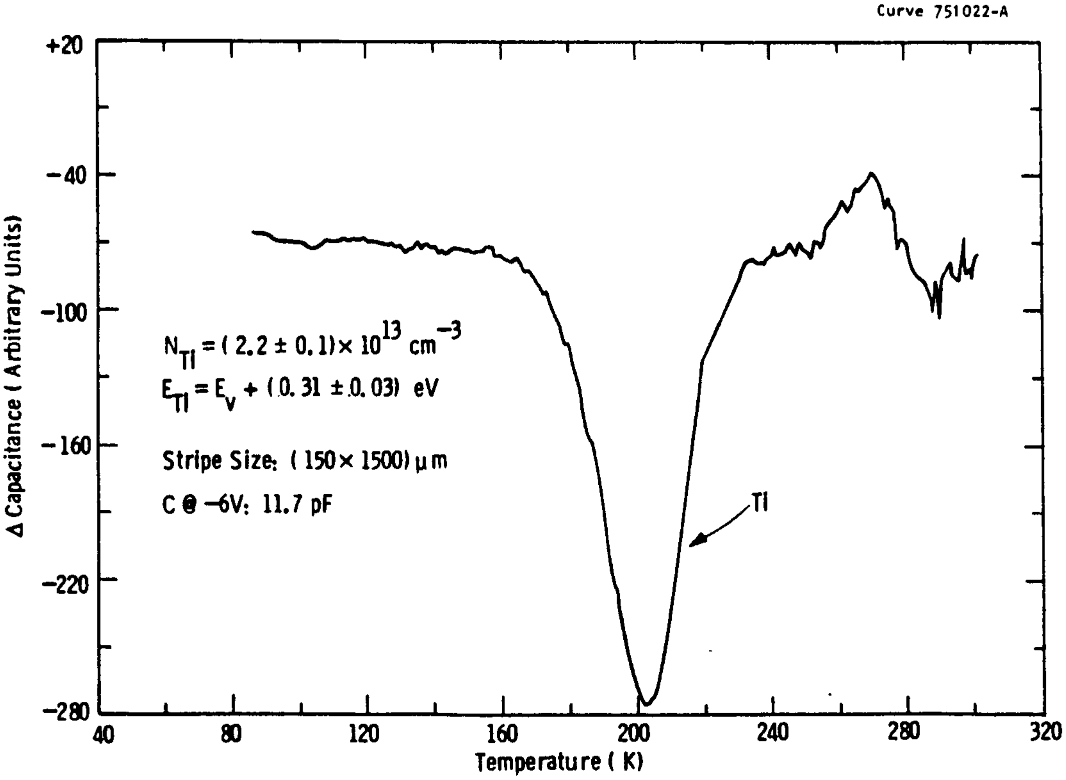

Figure 26. DLTS scan (C_{56}) for a Schottky diode (stripe) on the beveled surface of a smple prepared from an unprocessed Ti-doped CZ wafer (ingot 210-Ti, boron-doped to 4 ohm-cm). (Run TP-12, Sample #11, Stripe #2).

4. Program Status

4.1 PRESENT STATUS

The current milestone chart for this program is shown in Table 10. The major conclusions or observations that have been made during this reporting period are:

1. Previous conclusions regarding the strong correlation between cell efficiency (and diffusion length) and the density of dislocations and impurity precipitates have been confirmed.

2. Additional structural features have been observed in completed web cells by cross-sectional TEM, including the termination of twin lamellae within the bulk of the silicon, the asymmetric distribution of dislocations on one side of the heavily twinned region relative to the other side, and the climb of dislocations.

3. Modeling of the heavily twinned region, assumed to have a low (1 μm) diffusion length, shows that only when the diffusion length of the remainder of the bulk silicon exceeds the depth of the heavily twinned region is the presence of this region strongly felt. The measured efficiency and diffusion length of several web cells which were examined by TEM and LBIC agree well with the values calculated from the model.

4. Hydrogen ion implantation is effective in improving the efficiency (8.0% to 9.8% without AR coating) and diffusion length (23 μm to 58 μm) in web cells, provided appropriate implantation parameters are chosen. The best parameters found to date are an ion energy of

Table 10

Milestone Chart

		1985							1986				
		J	J	A	S	O	N	D	J	F	M	A	M
Task 1.	Investigate and reduce loss mechanisms in web	▲	─	─	─	─	─	─					
Task 2.	Employ gettering to improve bulk diffusion length to 150 μm or more.	▲	─	─	─	─	─	─					
Task 3.	Reduce surface recombination velocity to 10^4 cm/sec or less.	▲	─	─	─	─	─	─					
Task 4.	Provide samples to JPL to verify improved diffusion length and surface recombination velocity.			▲			▲			△			△
Task 5.	Refine cell design by model calculations.	▲	─	─	─	─	─	─					
Task 6.	Improve emitter performance by reducing heavy doping effects and by using polysilicon.	▲	─	─	─	─	─	─					
Task 7.	Improve cell efficiency by hydrogen passivation.	▲	─	─	─	─	─	─					
Task 8.	Deliver four web cells 4 cm^2 in area having the efficiencies indicated.			▲ (16.0%)			▲ (16.5%)			△ (17.0%)			△ (18.0%)
Task 9.	Support meetings.	As required by JPL											
Task 10.	Provide documentation.	▲	▲	▲	▲	▲	▲	▲	△	△	△	△	△

1500 eV, a beam current density of 2 mA/cm^2, and an implant time of two minutes.

5. Web cells (1 cm^2 in area) having the highest efficiency (17.3%) measured to date have been fabricated. This superior efficiency is attributed to high minority carrier diffusion length in the base (160 μm), an effective back-surface reflector (aluminum), and very low reflection losses (ZnS and MgF_2 AR coating).

6. A dot contact grid system has been designed in which the contact area between metal and silicon has been reduced by a factor of 40 for the front grid and by considerably more for the back contact. With this system, more than 99.9% of the front and back surfaces of the cell will be covered with a passivating oxide; less than 0.1% of the surface will have metal in direct contact with silicon.

7. Using CZ silicon that had been intentionally doped with titanium, the DLTS measurement technique has been verified for beveled samples which have been Sirtl etched.

4.2 FUTURE ACTIVITY

The effectiveness of hydrogen ion implantation into the emitter side of web strips immediately after the high-temperature diffusions will be investigated. The strips will be sufficiently large that full-sized cells (2.0 x 9.8 cm) can be made from the implanted material. The efficiency of cells made from these strips will be compared with the efficiency of cells made without hydrogen implantation. Low-resistivity (0.2 ohm-cm) web will be grown and hydrogen ion implantation will be used in an attempt to obtain base material which has both a low resistivity and a high diffusion length. Cells with an area of 4 cm^2 will be fabricated using the dot contact system. Modeling of the emitter will be done to obtain higher performance from this part of the cell. Included as parameters in the model will be junction depth (0.1, 0.2, and 0.3 μm), surface concentration (1 x 10^{19} and 1 x 10^{2} cm^{-3}), and dopant profile (flat, linear, and exponential).

5. References

1. M. Wolf, "Transport Velocity Transformation: A Convenient Method for Performance Analysis of Multilayer Solar Cell Structure," IEEE Trans. on Electron Devices, ED-28, 566 (1981).

2. D. L. Meier, A. Rohatgi, T. W. O'Keeffe, P. Rai-Choudhury, R. B. Campbell, and S. Mahajan, "Twin Plane Effects in Dendritic Web Silicon," Proceedings of the 18th IEEE Photovoltaic Specialists Conference, Las Vegas (1986).

3. P. Alexander and J. Crotty, Jet Propulsion Laboratory, private communication.

4. R. H. Hopkins et al., "Effects of Impurities and Processing on Silicon Solar Cells," Westinghouse Report 81-9F4-IMPUR-R3, 221 (February 1982).

6. Acknowledgments

The authors gratefully acknowledge C. W. Hughes for preparation of the TEM samples; M. Wolf of the University of Pennsylvania for providing the computer code for the solar cell modeling program; J. Spitznagel for making available the hydrogen ion implantation system; W. C. Chalmers for implanting the web cells; R. B. Campbell of Westinghouse AESD for the baseline cells; J. B. McNally, F. S. Youngk, P. Palaschak, and R. J. Fiedor for processing and measurement of the solar cells; L. E. Hohn for model calculations; B. A. Blankenship for the evaporation of the antireflection coatings; M. G. Markle for typing; and G. S. Law for document preparation.

FLAT PLATE SOLAR ARRAY PROJECT

Contractor Quarterly, Annual, Interim, and Final Report Distribution List

Distribution List #645 - Materials & Devices Area
(Total = 37 Copies)

	No. of copies
Applied Solar Energy Corporation Attn: D. C. Leung 15251 East Don Julian Road City of Industry, CA 91746	1
Electric Power Research Institute Attn: E. A. De Meo 3412 Hillview Avenue P. O. Box 10412 Palo Alto, CA 94304	1
Jet Propulsion Laboratory Attn: (Contract Negotiator) M/S 511-303 4800 Oak Grove Drive Pasadena, CA 91109	1
Jet Propulsion Laboratory Attn: Solar Data Library M/S 502-414 4800 Oak Grove Drive Pasadena, CA 91109	15
Jet Propuslion Laboratory Technology Utilization Attn: L. P. Speck M/S 180-302 4800 Oak Grove Drive Pasadena, CA 91109	1
Materials Research, Inc. Attn: Dr. Ram Natesh 790 East 700 South Centerville, UT 84014	1
NASA Headquarters Solar Terr. Systems Div. Attn: Donald Calahan 600 Independence Ave., SW Washington, DC 20546	1

	No. of copies
NASA Headquarters Attn: J. P. Mullin, Code RP-6 M/S B636 Washington, DC 20546	1
Research Triangle Institute Center for Semiconductor Research Attn: M. F. Lamorte P.O. Box 12194 Research Triangle Park, NC 27709	1
C. T. Sah Associates Attn: Dr. C. T. Sah 403 Pond Ridge Lane Urbana, Il 61801	1
Solar Energy Research Institute Attn: SEIC/LIBRARY 1617 Cole Blvd. Golden, CO 80401	1
Solar Energy Research Institute Photovoltaic Program Office Attn: Dr. Tom Surek 1617 Cole Boulevard Golden, CO 80401	1
University of Florida Attn: F. A. Lindholm 219 Ginter Hall Gainsville, FL 32611	1
University of Pennsylvania Attn: Prof. Martin Wolf 308 Moore D2 Philadelphia, PA 19174	1
University of Washington Joint Center for Graduate Study Attn: Dr. L. C. Olsen 100 Sprout Road Richland, Washington 99352	1

	No. of copies
U. S. Department of Energy Forrestal Building Attn: R. H. Annan 1000 Independence Ave., SW Washington, DC 20585	1
U. S. Department of Energy Forrestal Building Attn: Dr. Morton Prince M/S 5G026 Photovoltaic Energy Systems 1000 Independence Ave., SW Washington, DC 20585	1
U. S. Department of Energy Forrestal Building Attn: Anthony Scolaro Photovoltaic Energy Systems 1000 Independence Ave., SW Washington, DC 20585	1
U. S. Department of Energy Technical Information Center Attn: Doc. Control & Eval. Branch P. O. Box 62 Oak Ridge, TN 37830	2 + Repro
Westinghouse Electric Corporation Research Laboratories Attn: Dr. P. Rai-Choudhury 1310 Beulah Road Pittsburgh, PA 15235	1
Westinghouse Electric Corporation Research Laboratories Attn: D. L. Meier 1310 Beulah Road Pittsburgh, PA 15235	1